Mechanical Systems and Signal Processing 226 (2025) 112354

Contents lists available at ScienceDirect

Mechanical Systems and Signal Processing

journal homepage: www.elsevier.com/locate/ymssp

Full Length Article

Modeling and validation of a tri-section beam based multi-directional galloping energy harvester

Cuipeng Xia [a], Lihua Tang [a,*], Yi Wu [a], Guobiao Hu [b], Peilun Yin [a], Kean C. Aw [a], Daniel J. Inman [c]

[a] *Department of Mechanical and Mechatronics Engineering, The University of Auckland, Auckland 1010 New Zealand*
[b] *Internet of Things Thrust, The Hong Kong University of Science and Technology (Guangzhou), Guangzhou, Guangdong 511400, China*
[c] *Department of Aerospace Engineering, University of Michigan, Ann Arbor, MI 48109, United States*

ARTICLE INFO

Keywords:
Tri-section beam
Multi-directional
Galloping energy harvester
Global mode method
Computational fluid dynamics
Fully coupled aero-electro-mechanical model

ABSTRACT

A conventional galloping-based wind energy harvester is typically restricted to capturing energy from a single wind direction, making it inefficient in the unpredictable conditions of natural environments. This research presents comprehensive theoretical modeling of a novel galloping-based piezoelectric energy harvester featuring a tri-section beam structure to harvest wind energy from different flow directions by utilizing various vibrational modes. First, the global mode method (GMM) is employed to derive the natural frequencies and mode shapes, validated by comparison with the finite element method (FEM). Computational fluid dynamics (CFD) simulation is then conducted to analyze the aerodynamic characteristics of the bluff body under different incident wind directions, providing essential transverse aerodynamic force coefficients. With these modal parameters and aerodynamic coefficients, subsequently, the fully coupled aero-electro-mechanical model is established to evaluate the energy harvesting performance with varying wind speed and direction. The results show that the developed tri-section beam based galloping energy harvester can effectively capture wind energy from multiple directions with different vibration modes being triggered. The established theoretical model can successfully predict the triggering of different modes and accurately evaluate the electrical outputs in different wind conditions, which are validated by wind tunnel experiments. In addition, it is found that higher voltage and power outputs are achieved when galloping is triggered in the second order bending mode with a higher cut-in wind speed, as compared to the first order bending mode. The modelling and design of the developed multi-directional galloping energy harvester offers a feasible approach for harnessing flow energy in natural environments with unknown, varying wind conditions.

1. Introduction

The past few years have witnessed the pervasive integration of emerging microelectronic and portable devices into infrastructure and daily life. A diverse array of technologies, including wireless sensor networks, implantable medical devices, maritime communication buoys, and structural health monitoring systems, share a common requirement: a sustainable energy source for their

---

* Corresponding author.
E-mail address: l.tang@auckland.ac.nz (L. Tang).

https://doi.org/10.1016/j.ymssp.2025.112354
Received 15 September 2024; Received in revised form 13 December 2024; Accepted 12 January 2025

Nomenclature

d_s	Thickness of the substrate layer of the beam
d_p	Thickness of the piezoelectric transducer
b_s	Width of the substrate layer of the beam
b_p	Width of the piezoelectric transducer
L_p	Length of the piezoelectric transducer
L_i	Length of the *i*-th beam segment
D_1	Width of the splitter
D_2	Height of the splitter
W	Width of the bluff body
h	Height of the bluff body
l	Incident wind width of the bluff body
h_sn	Distance from the neutral axis to the top of the substrate layer of the beam
h_pn	Distance from the neutral axis to the bottom of piezoelectric transducer of the beam
h_a	Position of the bottom of piezoelectric transducer from the neutral axis
h_b	Position of the bottom of the substrate layer of the beam from the neutral axis
h_c	Position of the top of the substrate layer of the beam from the neutral axis
$w_i(x_i, t)$	Vertical deflection of *i*-th beam segment beam at x_i in the *i*-th local coordinate system
$w'_i(x_i, t)$	Angular displacement of *i*-th beam segment at x_i in the *i*-th local coordinate system
$u_i(x_i, t)$	Axial displacement of *i*-th beam segment beam at x_i in the *i*-th local coordinate system
$M_i(x_i, t)$	Moment of the *i*-th beam segment at x_i in the *i*-th local coordinate system
$Q_i(x_i, t)$	Shear force of the *i*-th segment beam at x_i in the *i*-th local coordinate system
$N_i(x_i, t)$	Axial force of the *i*-th segment beam at x_i in the *i*-th local coordinate system
I_i	Area moment of inertia of the *i*-th beam segment
E_iI_i	Bending stiffness of *i*-th beam segment
E_s	Young’s module of the substrate layer of the beam
E_p	Young’s module of the piezoelectric transducer
I_p	Area moment of inertia of the piezoelectric transducer
I_s1	Area moment of inertia of the first substrate beam
A_i	Cross-sectional area of the *i*-th segment beam
m_i	Distributed mass of the *i*-th segment beam
M_t	Mass of the bluff body
J_t	Mass moment of inertia of the bluff body
φ	Crease angle of the tri-section beam
A_p	Cross-sectional area for the piezoelectric transducer
A_s1	Cross-sectional area for the first substrate layer of the beam
$\psi_\mathrm{ir}(\mathrm{x})$	The *r*-th mode shape in the axial direction of *i*-th beam segment
$\phi_\mathrm{ir}(\mathrm{x})$	The *r*-th mode shape in the vertical direction of *i*-th beam segment
$q_r(t)$	The *r*-th modal coordinate
a_{ir}, b_{ir}, c_{ir}, d_{ir}	Coefficients of the *r*-th mode shape of the *i*-th beam segment in the vertical direction
g_{ir}, h_{ir}	Coefficients of the *r*-th mode shape of the *i*-th beam segment in the axial direction
δ_{ir}	Parameter related to the *r*-th natural frequency for *i*-th beam segment in the vertical direction
β_{ir}	Parameter related to the *r*-th natural frequency for *i*-th beam segment in the axial direction
ω_r	The natural frequency of *r*-th mode
U	Incident wind speed
u_x, u_y	the *x*- and *y*-components of the flow velocity in the Cartesian coordinate system
C_{Fy}	Transverse aerodynamic force coefficient
C_1, C_3, C_5	Polynomial fitting coefficients of C_{Fy}
θ	Incident wind direction
δ	Wind attack angle
ρ	Air density
U_{cr}	Cut-in wind speed
ε_{xx}	Strain of the beam in the axial direction
σ_s	Stress of the substrate layer of the beam in the axial direction
ρ_p	Density of the piezoelectric transducer
ρ_s	Density of the substrate layer of the beam
V_p	Volume of the piezoelectric transducer
V_s	Volume of the substrate layer of the beam
A_sj	Cross-sectional aera of the *j*-th substrate layer of the beam

σ_1	Stress for piezoelectric transducer
D_3	Electric displacement in the z direction
ε_1	Strain of the piezoelectric transducer in the x direction
E_3	Electric field in the z direction
$\overline{\mathrm{c}}_{11}^{\mathrm{E}}$	Elastic module of the piezoelectric transducer
$\overline{\mathrm{e}}_{31}$	Effective piezoelectric stress constant
$\overline{\varepsilon}_{33}^{\mathrm{S}}$	Permittivity constant
$V(t)$	Voltage across the piezoelectric transducer
T_{k}	Kinetic energy of the system
U_{p}	Potential energy of the system
W_{ie}	Internal electrical energy
W_{nc}	Non-conservative virtual work
C_{p}	Internal capacitance of the piezoelectric transducer
$\widetilde{\chi}_{\mathrm{r}}^{\mathrm{a}} - \widetilde{\chi}_{\mathrm{r}}^{\mathrm{b}}$	Electromechanical coupling term of the r-th vibrational mode
$Q(t)$	Electric charge output of the piezoelectric transducer
V_{OC}	Open circuit voltage
R_L	External load resistance
$\widetilde{\lambda}_1$, $\widetilde{\lambda}_2$	Coupling term of first and second vibrational mode
$\widetilde{M}_1$, $\widetilde{K}_1$, $\widetilde{\mathrm{C}}_1$	Modal mass, stiffness and damping of the first bending mode
$\widetilde{M}_2$, $\widetilde{K}_2$, $\widetilde{\mathrm{C}}_2$	Modal mass, stiffness and damping of the second bending mode
n	Young's module ratio of the substrate layer of the beam to the piezoelectric transducer
ξ_1, ξ_2	Damping ratios of the first and second bending mode
ω_1, ω_2	Natural frequencies of the first and second bending mode
$\widehat{\mathrm{a}}_0$, $\widehat{\mathrm{a}}_1$	Mass-proportional and stiffness-proportional damping coefficients

operations [1–3]. Chemical batteries have traditionally dominated as the primary energy source for these applications; however, their widespread adoption faces significant challenges due to their finite operational lifespan and the deleterious ecological consequences associated with their production, use, and disposal [4]. Significant advancements in the development of microelectromechanical systems (MEMS) have led to a considerable decrease in the power consumption of electronic devices [5]. This reduction in energy requirements has stimulated a viable and promising opportunity to exploit the energies abundant in the ambient environment for powering a multitude of small electronic devices [6,7]. The surrounding environment encompasses a variety of renewable energy sources, such as vibrations [8,9], tidal energy [10], wind flow [11,12], solar energy [13], and waste heat [14]. Among them, vibration energy existing in different forms has garnered significant interest and numerous conversion mechanisms exist to transform it into electricity, including electromagnetic induction [15], piezoelectricity [16–18], and triboelectrification [19–21].

For traditional vibration-based energy harvesting, multi-modal designs are one solution to overcome the limitation of the narrow operational frequency bandwidth of conventional single-degree-of-freedom energy harvesters. Li et al. [22] introduced a multi-modal piezoelectric energy harvester design that featured a main cantilevered beam coupled with three branch beams to achieve three close resonant modes. Dhote et al. [23] introduced a multi-mode energy harvester design featuring an orthoplanar spring structure for multiple closely spaced resonant peaks. L-shaped beam structures are extensively investigated to achieve broad bandwidth [24–28]. By carefully modifying the system parameters, such as introducing side and end tip masses, as well as varying the lengths of the two beams to realize different internal resonance ratios, the overall energy harvesting performance of the system can be enhanced. For instance, Nie et al. [24] investigated the performance of an L-shaped piezoelectric energy harvester by adjusting the side and end masses to achieve a two-to-one internal resonance for broadband and enhanced energy output. On the other hand, ambient vibrations could occur in multiple directions, and most of the reported vibration energy harvesters typically operated when subjected to excitation in a specific direction. Researchers have also devoted their efforts to addressing the limitation of unidirectional sensitivity, including the incorporation of orthogonally configured oscillators [29], combinations of oscillator arrays [30], elastic oscillators with multiple degrees of freedom [31], fabricating the internal resonance [32,33] and pendulum system [34–37]. Fan et al. [30] explored the characteristics of a U-shaped vibration-based energy harvester, which exhibited the capability to achieve the closer first two vibrational modes and can operate in two orthogonal directions via a two-to-one internal resonance. Xing et al. [35] proposed a novel multi-directional broadband piezoelectric energy harvester featuring a zigzag beam and a rigid pendulum. Numerical and experimental results demonstrated that the system could achieve good energy harvesting performance via internal resonances in three orthogonal directions. Zhang et al. [36] introduced a piezoelectric energy harvester with a pendulum mechanism, in which the swinging motion of the pendulum was coupled with the bending action of the cantilever beam, enabling effective multidirectional energy harvesting from various vibrational sources. Kan et al. [37] developed a low-frequency multidirectional vibrational energy harvester, incorporating a multidirectional universal joint that links a pendulum to a conventional piezoelectric beam. The motion of the universal joint, induced by the simple pendulum, indirectly plucked the piezoelectric beams of the harvester. Furthermore, the universal joint's ability to generate rolling motion at arbitrary angles enabled the harvester to detect vibrations from multiple directions. Both theoretical and experimental results confirmed the device's effectiveness in capturing multidirectional vibrational energy. Lu et al. [38] fabricated a tunable buckled piezoelectric energy harvester to capture vibrations in multiple directions with two separate vibration modes, showing a significant improvement in energy harvesting efficiency compared to the single-direction buckling mode configuration. Chen et al. [39] introduced an M−shaped piezoelectric energy harvester design featuring nonlinear orthogonal elements to enable the effective extraction of vibrational energy from the environment. The internal resonance design induced mutual excitation of vibrations in both the horizontal and vertical directions, thereby ensuring the capability of scavenging multi-directional ambient vibration energy. Wu et al. [40] designed a piezoelectric energy harvester with a single-stack and a rhombus-type force amplifier combined with a selectivity lever to harvest both pull and push bidirectional energy. The experimental results indicated that the proposed harvester had the merits of a high safety factor and compact size to scavenge vibrational energy efficiently. Tan et al. [41] introduced an auto-parametric internal resonant system coupled with a nonlinear energy sink, aimed at enhancing both dynamic and directional responses for piezoelectric vibration energy harvesting. Zeng et al. [42] introduced an innovative bistable wave energy harvester featuring directional self-adaptation. This design leverages the collision between a driving ball and the generator beam to convert multidirectional, ultra-low-frequency wave motions into localized high-frequency oscillations.

Recognized as one of the most prevalent renewable energy sources, wind has been extensively utilized for energy harvesting through its conversion into vibrations, leveraging various aeroelastic instability mechanisms, such as galloping [43–45], wake galloping [46,47], vortex-induced vibrations (VIV) [48–50], wake VIV [51,52], and flutter [53,54]. Among them, extensive research has been conducted on mechanisms involving vortex-induced vibrations (VIV) and galloping phenomena. It is noteworthy that a VIV-based energy harvesters can achieve efficient operation when the vortex shedding frequency matches the natural frequency of the harvester [55], which means that this optimal performance is limited due to the lock-in wind speed range. In the natural environment, wind direction and speed typically vary over time. To expand the operational range and improve output performance, Wang et al. [56] introduced a cross-coupled dual-beam VIV energy harvester design featuring a cylindrical bluff body supported by two series-connected beams with perpendicular bending directions. However, the design is limited to functioning in only two incident wind directions. Su and Lin [57] developed a VIV-based wind energy harvester featuring a U-shaped supporter to expand the range of incident wind directions and confirmed its ability of collecting wind energy from two orthogonal directions. Li et al [58] developed a VIV piezoelectric wind energy harvester featuring a cylindrical shell, which could adapt to omnidirectional incident wind due to its geometric characteristics. Both simulations and experimental results indicated that the impact of wind direction on the total power output is minimal. Gong et al [59] introduced a direction-adaptive VIV-based energy harvester equipped with a guide wing to capture flow energy. Experimental findings showed that the prototype could effectively operate over an extended range of incident wind directions in a single vibration mode. Zhang et al. [60] and Meng et al. [61] developed a novel spherical bluff body to scavenge wind energy from multiple directions based on VIV. While these reported VIV-based harvesters could operate in various directions, they only performed effectively in a narrow wind speed range (lock-in region) with a single vibration mode, thereby restricting their overall efficiency and output.

In addition to VIV, other researchers have concentrated on galloping-based wind energy harvesters, which possess the property of increasing oscillation amplitude with rising wind speed, thereby providing useful output across a broad wind speed range [62]. The bluff body is crucial in improving the performance of galloping piezoelectric energy harvesters. Xing et al [63] explored the potential effect of implementing different bluff body surface protrusions, and both experimental and simulation results indicated that elliptical protrusions offered the outstanding potential for enhancing galloping energy harvesting performance. Wang et al. [64,65] discovered that bluff bodies with isosceles triangle sections and Y-shaped attachments could significantly improve the performance of piezoelectric galloping energy harvesters. Cui et al. [66] investigated the galloping behavior of an iced bundled bluff body using simultaneous measurement techniques. This novel approach allowed for the examination of the spatial galloping behavior across various vibrational modes. However, the galloping behavior of non-circular bluff body is sensitive to the incident wind direction, which was not received much attention in the reported literature. Additionally, the use of a normal straight beam restricts the operational range of incident wind directions for galloping-based harvesters, like the VIV-based harvesters. Some researchers have focused on designing galloping-based wind energy harvesters to accommodate varying incident wind direction. Lu et al. [67] employed a piezoelectric composite cantilever and a multi-tooth bluff body to harness multi-directional wind energy through galloping. However, this design could only capture wind energy in a single vibrational mode. Sun et al. [68] introduced a wind-direction adaptive piezoelectric energy harvester featuring a small wing passive control configuration and established a criterion to assess the impact of wind direction change on energy harvesting efficiency. Nevertheless, the galloping-based harvester is limited to scavenging energy in straightforward bidirectional wind conditions. Lim et al. [69] developed a self-tunable galloping-based energy harvester featuring a rotating base and vane to capture energy from multiple incident wind directions. However, experimental results showed that the rotating base configuration led to a higher cut-in speed, possibly due to the damping effect during the base’s angular movement, which negated the energy harvesting potential.

Despite the existence of various approaches and systems for galloping energy harvesting in multiple incident wind directions, it is noteworthy that there is limited research on harvesters capable of executing multi-directional energy harvesting from multi-modal vibrations. In our preliminary experimental work [70], a galloping-based energy harvester with tri-section beam was proposed to scavenge wind energy from multiple directions, and the concept was only confirmed in wind tunnel tests. However, comprehensive theoretical modeling has yet to be conducted to assist the understanding of dynamic characteristics and prediction of electrical output performance. This work aims to bridge this gap by systematic modeling to aid the performance prediction of such tri-section beam based galloping energy harvester. The remainder of this study is organized as follows. In Section 2, the global modal method is first formulated theoretically to solve the eigenvalue problem, thereby obtaining the natural frequencies and mode shapes, validated by the finite element method (FEM). Section 3 presents the aerodynamic characteristics of a bluff body with splitters under different incident wind directions and analyzed via computational fluid dynamics (CFD). With the derived modal parameters and aerodynamic force coefficients, in Section 4, a fully coupled aero-electro-mechanical model is formulated. Section 5 presents the physical prototype design

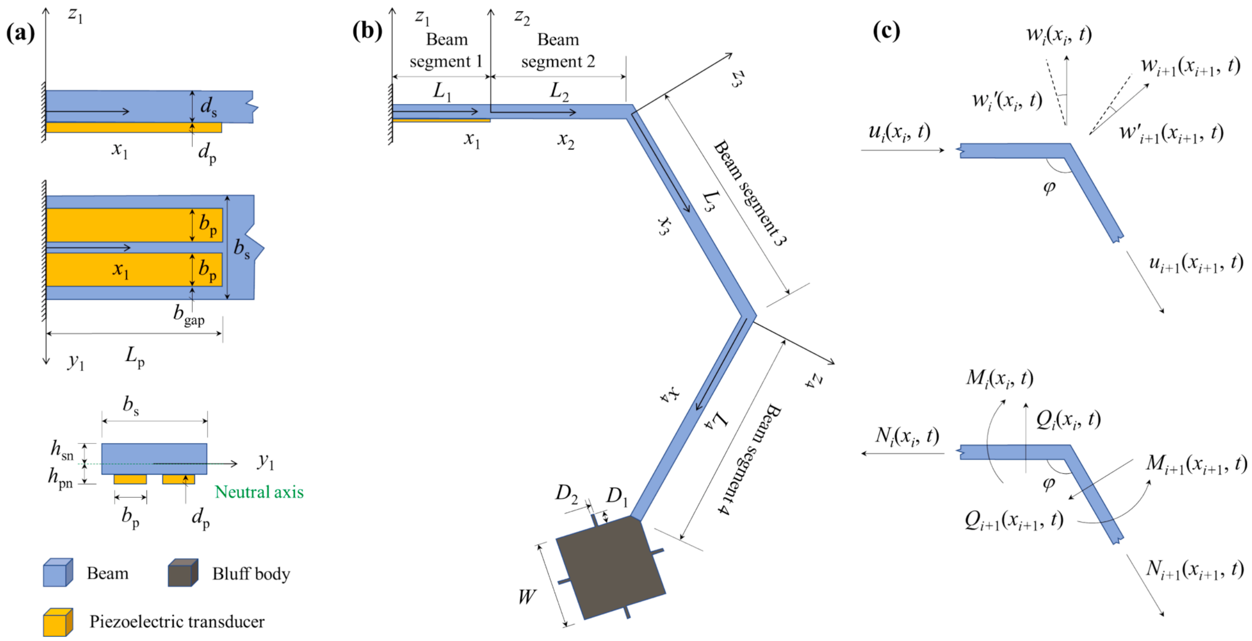

Fig. 1. Multi-directional galloping-based piezoelectric energy harvester with tri-section beam. (a) geometrical parameters of the substrate layer and piezoelectric transducers, (b) local coordinate systems of the beam segments, and (c) boundary conditions at the connecting point.

Table 1
Geometric and material properties of the proposed harvester.

Properties	Beam	MFC	Unit	Properties	Bluff body	Unit
Length	180	37	mm	Edge width (W)	35	mm
Width	30	11	mm	Height (h)	140	mm
Thickness	1.5	0.3	mm	Splitter dimensions ($D_1 \times D_2$)	5 × 1.5	mm
Apparent Density	1300	7800	Kg·m^{-3}	Apparent Density	248.8	Kg·m^{-3}
Young's modulus	2.1	30.3	GPa	Young's modulus	2.1	GPa
Poisson's ratio	0.3	0.33	/	Poisson's ratio	0.3	/

and the wind tunnel test setup. In Section 6, following the experimental validation of the theoretical model, the dynamic/aerodynamic characteristics and electrical output performance of the developed multi-directional galloping-based energy harvester are discussed in detail. Section 7 summarizes the main findings from this work.

2. Modal analysis

2.1. Geometric configuration

The schematic of the proposed multi-directional galloping-based piezoelectric energy harvester is shown in Fig. 1, comprising a cantilevered tri-section beam and a square bluff body attached at its tip. Four splitters are affixed to the center of four side facets of the bluff body to augment its tendency of aerodynamic instability. The first section of the beam comprises two segments with and without piezoelectric transducer and are designated as L_1, L_2, and the other two sections as L_3, and L_4, with the respective lengths of 37 mm, 23 mm, 60 mm, and 60 mm. The crease angle φ between two adjacent beam sections is $2\pi/3$ rad. The beam and the bluff body were 3D-printed with Polylactic Acid (PLA), with different infill percentages selected for different components. Two piezoelectric transducers (Macro Fiber Composite (MFC) from Smart Material Corporation), as shown in Fig. 1(a), are bonded to the beam section in proximity to the clamped end due to the higher strain experienced in this region compared to other beam sections, as confirmed by FEM simulations, which are not presented here for brevity. Fig. 1(a) also illustrates the neutral axis of the beam cross-section, while the detailed dimensions of this section are elucidated in Appendix A. The geometric and material properties of the proposed harvester are shown in Table 1.

2.2. Eigenvalue problem formulation

To derive the fully coupled model for the multi-directional galloping-based energy harvester with tri-section beam in Section 4, accurate global mode shapes should be determined, and the natural frequencies should be derived. Wei et al. [71] introduced the global mode method (GMM) transforming the system's partial differential equations into ordinary differential equations and the simulation results revealed that the implementation of the global modal method exhibited superior accuracy compared to assumed mode method [72]. Yi et al. [73] formulated the mathematical model of a multi-beam ring structure based on the GMM and their natural frequencies and mode shape results exhibited excellent agreement with the finite element results as the global modes acquired through this method can faithfully represent the actual deformations of the system. Inspired by their result, we perform the modal analysis of the proposed energy harvester with the multi-section beam by using GMM. The local coordinate system for each individual beam segment is illustrated in Fig. 1(b). The origin of the local coordinate system is set at the start of each beam segment, with the x_i and y_i representing the longitudinal and lateral directions of the i-th beam segment, respectively. The distributed parameter model is derived based on Euler-Bernoulli beam theory for these slender beam segments. The internal axial force, shear force and bending moment, and the axial displacement, transverse deflection and angular displacement at the position x_i of the i-th beam segment can be rewritten as $N_i(x_i,t)$, $Q_i(x_i,t)$, $M_i(x_i,t)$, $u_i(x_i,t)$, $w_i(x_i,t)$ and $w_i'(x_i,t)$, as shown in Fig. 1(c). Apart from the boundary conditions at the clamped end and the tip of the beam, the deflections at connecting points of neighboring segments must be equal, and the forces and moments acting on connecting points should be balanced. All boundary conditions are detailed in Equations (1)-(24) as follows:

$$w_1(x_1,t)|_{x_1=0} = 0 \tag{1}$$

$$\frac{\partial w_1(x_1,t)}{\partial x_1}|_{x_1=0} = 0 \tag{2}$$

$$w_1(x_1,t)|_{x_1=L_1} = w_2(x_2,t)\big|_{x_2=0} \tag{3}$$

$$\frac{\partial w_1(x_1,t)}{\partial x_1}|_{x_1=L_1} = \frac{\partial w_2(x_2,t)}{\partial x_2}\Big|_{x_2=0} \tag{4}$$

$$w_2(x_2,t)|_{x_2=L_2} = -w_3(x_3,t)|_{x_3=0}\cos\varphi - u_3(x_3,t)\Big|_{x_3=0}\sin\varphi \tag{5}$$

$$\frac{\partial w_2(x_2,t)}{\partial x_2}|_{x_2=L_2} = \frac{\partial w_3(x_3,t)}{\partial x_3}\Big|_{x_3=0} \tag{6}$$

$$w_3(x_3,t)|_{x_3=L_3} = -w_4(x_4,t)|_{x_4=0}\cos\varphi - u_4(x_4,t)\Big|_{x_4=0}\sin\varphi \tag{7}$$

$$\frac{\partial w_3(x_3,t)}{\partial x_3}|_{x_3=L_3} = \frac{\partial w_4(x_4,t)}{\partial x_4}\Big|_{x_4=0} \tag{8}$$

$$u_1(x_1,t)|_{x_1=0} = 0 \tag{9}$$

$$u_1(x_1,t)|_{x_1=L_1} = u_2(x_2,t)\big|_{x_2=0} \tag{10}$$

$$u_2(x_2,t)|_{x_2=L_2} = -u_3(x_3,t)|_{x_3=0}\cos\varphi + w_3(x_3,t)\Big|_{x_3=0}\sin\varphi \tag{11}$$

$$u_3(x_3,t)|_{x_3=L_3} = -u_4(x_4,t)|_{x_4=0}\cos\varphi + w_4(x_4,t)\Big|_{x_4=0}\sin\varphi \tag{12}$$

where $w_i(x_i,t)$ and $u_i(x_i,t)$ ($i = 1, 2, 3, 4$) denote transverse deflections and axial displacements of the i-th beam segment in their respective local coordinate systems.

$$E_1I_1\frac{\partial^2 w_1(x_1,t)}{\partial x_1^2}|_{x_1=L_1} = E_2I_2\frac{\partial^2 w_2(x_2,t)}{\partial x_2^2}\Big|_{x_2=0} \tag{13}$$

$$E_1I_1\frac{\partial^3 w_1(x_1,t)}{\partial x_1^3}|_{x_1=L_1} = E_2I_2\frac{\partial^3 w_2(x_2,t)}{\partial x_2^3}\Big|_{x_2=0} \tag{14}$$

$$E_2I_2\frac{\partial^2 w_2(x_2,t)}{\partial x_2^2}|_{x_2=L_2} = E_3I_3\frac{\partial^2 w_3(x_3,t)}{\partial x_3^2}\Big|_{x_3=0} \tag{15}$$

$$E_2I_2\frac{\partial^3 w_2(x_2,t)}{\partial x_2^3}|_{x_2=L_2} = -E_3I_3\frac{\partial^3 w_3(x_3,t)}{\partial x_3^3}|_{x_3=0}\cos\varphi + E_3A_3\frac{\partial u_3(x_3,t)}{\partial x_3}\Big|_{x_3=0}\sin\varphi \tag{16}$$

$$E_3I_3\frac{\partial^2 w_3(x_3,t)}{\partial x_3^2}|_{x_3=L_3} = E_4I_4\frac{\partial^2 w_4(x_4,t)}{\partial x_4^2}\Big|_{x_4=0} \tag{17}$$

$$E_3I_3\frac{\partial^3 w_3(x_3,t)}{\partial x_3^3}|_{x_3=L_3} = -E_4I_4\frac{\partial^3 w_4(x_4,t)}{\partial x_4^3}|_{x_4=0}\cos\varphi + E_4A_4\frac{\partial u_4(x_4,t)}{\partial x_4}\Big|_{x_4=0}\sin\varphi \tag{18}$$

$$E_4I_4\frac{\partial^2 w_4(x_4,t)}{\partial x_4^2}|_{x_4=L_4} = -J_{\mathrm{t}}\frac{\partial^3 w_4(x_4,t)}{\partial x_4\partial t^2}\Big|_{x_4=L_4} \tag{19}$$

$$E_4I_4\frac{\partial^3 w_4(x_4,t)}{\partial x_4^3}|_{x_4=L_4} = M_{\mathrm{t}}\frac{\partial^2 w_4(x_4,t)}{\partial t^2}\Big|_{x_4=L_4} \tag{20}$$

$$E_1A_1\frac{\partial u_1(x_1,t)}{\partial x_1}|_{x_1=L_1} = E_2A_2\frac{\partial u_2(x_2,t)}{\partial x_2}\Big|_{x_2=0} \tag{21}$$

$$E_2A_2\frac{\partial u_2(x_2,t)}{\partial x_2}|_{x_2=L_2} = -E_3I_3\frac{\partial^3 w_3(x_3,t)}{\partial x_3^3}|_{x_3=0}\sin\varphi - E_3A_3\frac{\partial u_3(x_3,t)}{\partial x_3}\Big|_{x_3=0}\cos\varphi \tag{22}$$

$$E_3A_3\frac{\partial u_3(x_3,t)}{\partial x_3}|_{x_3=L_3} = -E_4I_4\frac{\partial^3 w_4(x_4,t)}{\partial x_4^3}|_{x_4=0}\sin\varphi - E_4A_4\frac{\partial u_4(x_4,t)}{\partial x_4}\Big|_{x_4=0}\cos\varphi \tag{23}$$

$$E_4A_4\frac{\partial u_4(x_4,t)}{\partial x_4}|_{x_4=L_4} = M_{\mathrm{t}}\frac{\partial^2 u_4(x_4,t)}{\partial t^2}\Big|_{x_4=L_4} \tag{24}$$

where E_i denotes the Young's modulus of the i-th beam segment, and A_i represents the cross-sectional area of the i-th beam segment, respectively. M_{t} and J_{t} are the mass and mass moment of inertia of the bluff body, respectively.

The closed-form solutions of the tri-section beam's transverse deflection and axial displacement can be represented as:

$$\begin{cases} w_i(x_i,t) = \sum_{r=1}^{\infty}\phi_{ir}(x_i)q_r(t) \\ u_i(x_i,t) = \sum_{r=1}^{\infty}\psi_{ir}(x_i)q_r(t) \end{cases} \tag{25}$$

where $\phi_{ir}(x_i)$ and $\psi_{ir}(x_i)$ represent the transverse deflection mode shape and axial displacement mode shape of the r-th mode of the i-th beam segment, respectively. $q_r(t)$ denotes the modal coordinate of the r-th mode. The steady-state response is considered by assuming $q_r(t) = e^{j\omega t}$. The general solutions of $\phi_{ir}(x_i)$ and $\psi_{ir}(x_i)$ take the forms as:

$$\phi_{ir}(x_i) = a_{ir}\sin\beta_{ir}x_i + b_{ir}\cos\beta_{ir}x_i + c_{ir}\sinh\beta_{ir}x_i + d_{ir}\cosh\beta_{ir}x_i \tag{26}$$

$$\psi_{ir}(x_i) = g_{ir}\sin\delta_{ir}x_i + h_{ir}\cos\delta_{ir}x_i \tag{27}$$

where the relationships between β_{ir}, δ_{ir} and ω_r are written as follows [74]:

$$\omega_r^2 = \frac{\beta_{ir}^4 E_iI_i}{m_i} = \frac{\delta_{ir}^2 E_iA_i}{m_i} \tag{28}$$

The vector $\mathbf{\Omega}$ of the 24 coefficients of the mode shape can be written as follows:

$$\mathbf{\Omega} = [\,\Re_{1r}\quad \Re_{2r}\quad \Re_{3r}\quad \Re_{4r}\quad \Im_{1r}\quad \Im_{2r}\quad \Im_{3r}\quad \Im_{4r}\,]^T \Re_{ir} = [\,a_{ir}\quad b_{ir}\quad c_{ir}\quad d_{ir}\,] \Im_i = [\,g_{ir}\quad h_{ir}\,] \tag{29}$$

Substituting Equations (26) and (27) into Equations (1)-(24), the resulting simultaneous equations (see Appendix B.1) can be arranged in the matrix form as:

$$\boldsymbol{H}(\omega)\mathbf{\Omega} = 0 \tag{30}$$

where $\mathbf{H}(\omega)$ is a 24x24 matrix (see Appendix B.2). For non-trivial solution of $\mathbf{\Omega}$, the determinant of $\mathbf{H}(\omega)$ should be zero, which leads to the transcendental characteristic equation. The natural frequencies of the system can be obtained by numerically solving the characteristic equation, denoted as ω_r (ω_1, ω_2, ω_3, …, ω_n, …) in the ascending order. By substituting ω_r into Equation (30) and obtaining $\mathbf{\Omega}$, the global mode shapes of the system can then be derived with the determined ω_r and $\mathbf{\Omega}$ in Equations (26)-(27).

2.3. Natural frequencies and mode shapes

Finite element method (FEM) based modal analysis using the commercial package ANSYS is employed to verify the derived mode

Table 2
Comparison of the natural frequencies of the first two bending modes from the FEM and the theoretical model.

Mode shape	ANSYS (Hz)	GMM (Hz)	Difference
Frist order bending mode	4.82	5.14	5.64 %
Second order bending mode	17.17	17.25	0.46 %

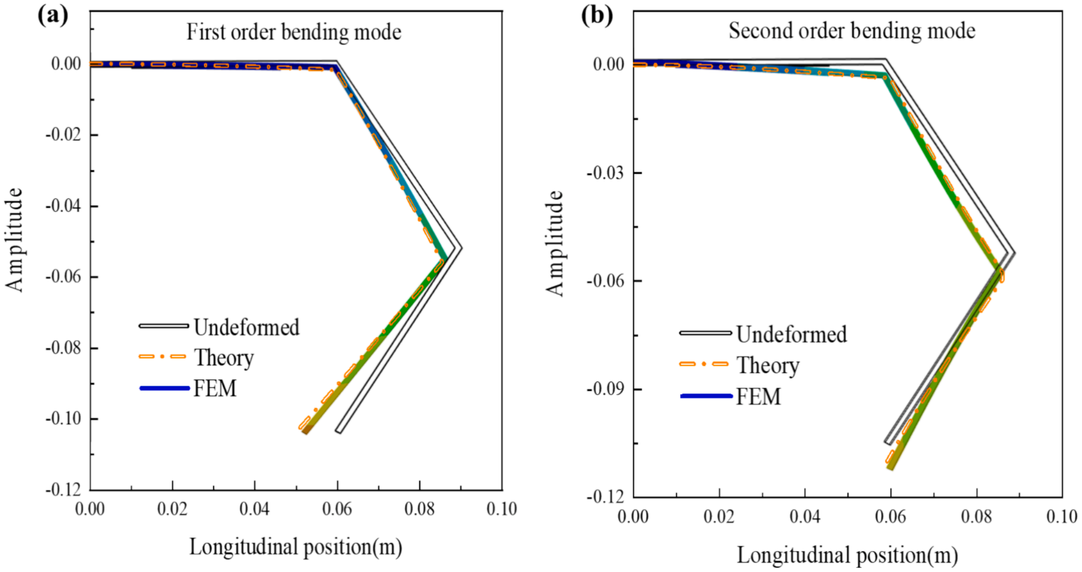

Fig. 2. Verification of the first two bending mode shapes: (a) first order bending mode and (b) second order bending mode.

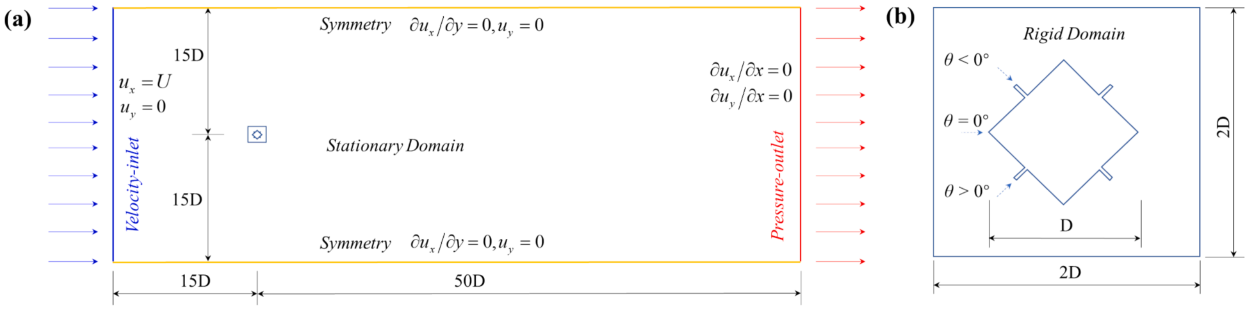

Fig. 3. Computation domain and boundary conditions: (a) Overall and (b) local domains.

shapes and corresponding natural frequencies in Section 2.2, and the results are listed in Table 2. The differences between the natural frequencies predicted by ANSYS and GMM are 5.64 % and 0.69 % for the first and second order bending modes. In addition, Fig. 2(a) and Fig. 2(b) depict the first and second order bending mode shapes obtained from the theory and FEM. In general, the theoretical results from GMM are in good agreement with the FEM results.

3. Aerodynamic analysis

In this section, CFD is utilized to investigate the aerodynamic characteristics of the bluff body and obtain the aerodynamic force to be used for the following fully coupled model that will predict the energy harvester's electric output performance. The following assumptions were made for the CFD simulation: the flow was considered incompressible, as the velocity was significantly below the speed of sound, leading to negligible density variations. Additionally, the pressure and temperature changes were sufficiently small to disregard compressibility effects, consistent with assumptions typically applied in low-speed aerodynamics. The 3D geometry can be simplified to a 2D model to analyze the aerodynamic characteristics of the bluff body. This simplification is justified as the 2D slice does not exhibit significant variation in the radial direction, making it suitable for analyzing aerodynamic lift and drag. The flow in the straight, long wind tunnel with a uniform cross-section supports the assumption of 2D behavior. Additionally, the 2D model offers

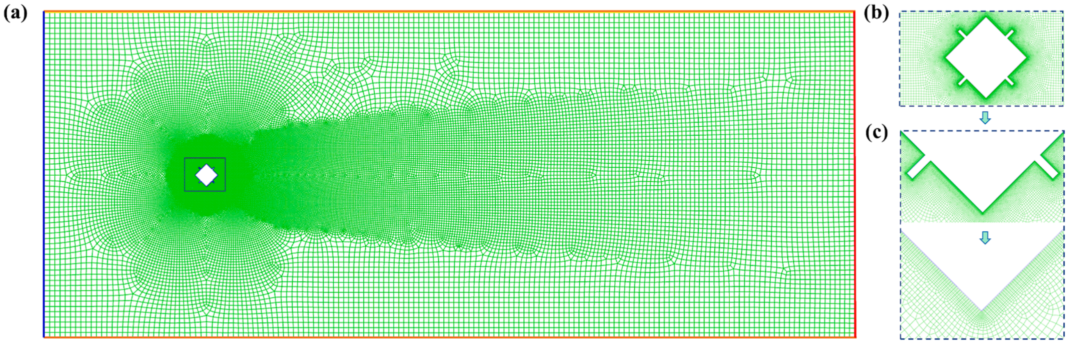

Fig. 4. Mesh generation in the computational domain and boundaries around the bluff body with splitters: (a) Overall meshing, (b) local meshing and (c) boundary layer meshing.

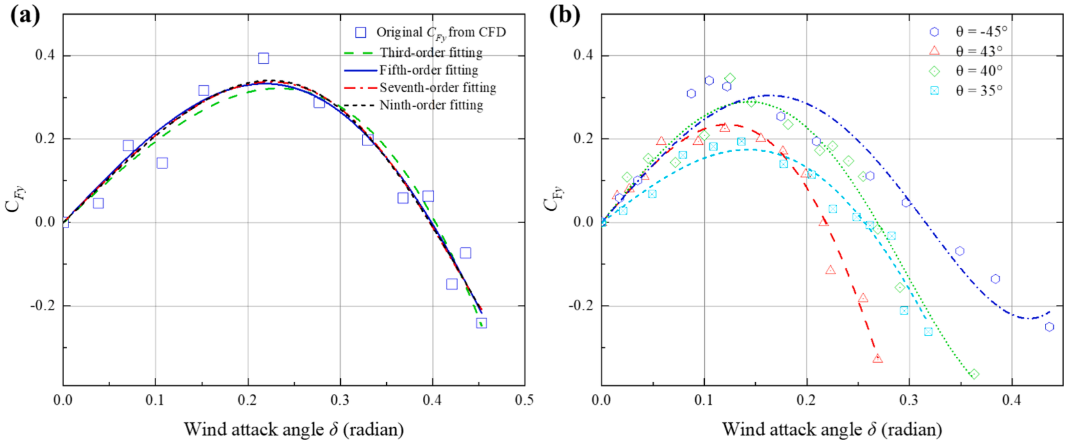

Fig. 5. (a) Comparison of different polynomial fittings of C_{Fy} with incident wind direction θ = -49° for the bluff body with splitters, and (b) fifth order polynomial fittings of C_{Fy} with different incident wind directions.

considerable computational efficiency, enabling a more resource-effective simulation without compromising the reliability of the results. The processes of meshing and calculation are detailed as follows. Fig. 3 shows the computational domain with dimensions of 65D × 30D, where D represents the diagonal length of the bluff body with splitters. In the computational domain, the left and right boundaries are designated as the velocity inlet (denoted in blue) and pressure outlet (denoted in red), respectively. The distances from the center of the bluff body to the inlet and outlet boundaries are 15D and 50D, respectively, while the distances to the upper and lower boundaries are both 15D. The dimensionless boundary conditions are illustrated in Fig. 3(a). The inlet boundary condition is set as a uniform flow with a constant velocity U. The variables u_x and u_y represent the x- and y-components of the flow velocity in the Cartesian coordinate system. A symmetric boundary condition is applied at two lateral sides (denoted in orange), where the normal velocity gradient and tangential velocities are zero ($\partial u_x/\partial y = 0$, $u_y = 0$). At the outlet boundary, the Neumann boundary condition is applied, implying that the normal velocity gradient in the x-direction is zero ($\partial u_x/\partial x = 0$, $\partial u_y/\partial x = 0$). No-slip boundary conditions were applied at the bluff body surface. This assumption ensures that the fluid velocity at the boundary is zero, accurately capturing the viscous effects near the wall. The two-dimensional computational domain (a 2D × 2D square rigid domain) is illustrated in Fig. 3(b), where the zero-incident wind direction (reference, $\theta = 0°$), positive and negative incident wind directions are shown.

In Fig. 4, the thickness of the first boundary layer around the bluff body surface is approximately 0.001D, and a growth factor of 1.08 is applied along the radial direction until the 10th boundary layer. An unstructured quadrilateral mesh, with the desirable properties, such as flexibility in geometry, local mesh reconstruction and refinement capability, is chosen for the remaining portion of the rigid computational domain. The remaining peripheral area of the computational domain is referred to as the stationary domain, which remains static during the simulation process, and the mesh type employed in this region is also an unstructured quadrilateral mesh. To improve the computational efficiency, the outer region is discretized with slightly coarser meshes. In this study, the total numbers of nodes and faces are 82,204 and 163,096, respectively. The k-ω shear stress transport (SST) turbulence model is employed to account for the low Reynolds number effects near the wall. Consequently, the viscous sublayer is modeled as the wall boundary condition and solved to obtain highly accurate results in the near-wall region and ensure that the maximum value of $y+$ for each grid scheme remains less than 1.

The commercial package ANSYS FLUENT is employed to simulate the flow and obtain the lift and drag force coefficients of the bluff

Table 3

Coefficients of the fifth-order polynomial fitting under five incident wind directions.

Incident wind direction θ	C_1	C_3	C_5
−49°	2.183	−15.31	10.46
−45°	2.871	−41.17	123.31
43°	2.926	−69.93	178.30
40°	3.108	−57.06	194.70
35°	1.871	−33.17	71.31

body. The k-ω SST turbulence model, formulated as a two-equation model, is adopted to relate the Reynolds stresses to the time-averaged variables. The finite volume method is employed to discretize the Reynolds-Averaged Navier-Stokes (RANS) governing equations in a second order formulation. The gradient term is discretized based on the least-squares cell-based method. The pressure term is discretized using a second order formulation, while the momentum, turbulent kinetic energy, and specific dissipation rate are discretized using the Quadratic Upstream Interpolation for Convective Kinematics (QUICK) scheme. The pressure–velocity coupling is achieved utilizing the Semi-Implicit Method for Pressure Linked Equation Consistent (SIMPLEC) algorithm.

According to the well-known Den Hartog criterion [75], galloping will occur when the first order derivative of the transverse aerodynamic force coefficient (C_{Fy}) is positive. The slope of the curve C_{Fy} versus the wind attack angle [70] δ (the angle between the incident wind direction and the bluff body's movement direction) at $\delta = 0^\circ$ can be written as follows:

$$\frac{\partial C_{Fy}}{\partial \delta}\Big|_{\delta=0^\circ} = -\left(\frac{\partial C_L}{\partial \delta} + C_D\right)\Big|_{\delta=0^\circ} > 0 \tag{31}$$

Fig. 5(a) shows the original transverse force coefficient of the square bluff body with splitters as a function of the wind attack angle, along with different orders of polynomial fitting curves, when the incident wind direction is θ = -49°. It is noted that C_{Fy} increases with δ, peaks at a certain angle, and then decreases. The slope of the fitting curves at a zero attack angle is positive, which implies that when the aerodynamic damping exceeds the structural damping, the system's total damping becomes negative, causing galloping to occur [44,63]. The coefficient of determination (R^2) for the third and fifth order polynomial fittings are 0.7891 and 0.9562, respectively, indicating that the quintic fitting is superior to the cubic fitting. The R^2 values for the higher-order fittings (0.9568 for the seventh-order and 0.9576 for the ninth-order) are nearly identical to that of the fifth-order fitting. Furthermore, the higher-order fittings demand excessive computational resources to solve the fully coupled aero-electro-mechanical governing equations. Other researchers [65,70] have also successfully employed the fifth order polynomial fitting ($C_{Fy} = C_1\delta + C_3\delta^3 + C_5\delta^5$) to interpret the relationship between the transverse force coefficient and the wind attack angle. Therefore, the fifth order polynomial fitting is utilized in our model for the incident wind directions of θ = -45°, 43°, 40°, and 35°, as shown in Fig. 5(b).

Table 3 tabulates the fifth-order polynomial fitting coefficients for the five different incident wind directions: θ = -49°, −45°, 43°, 40°, and 35°. When the incident wind direction is 35°, the linear aerodynamic coefficient C_1 exhibits the minimum value of 1.871. Meanwhile, the linear aerodynamic coefficient C_1 reaches its maximum value (3.108) for the incident wind directions of θ = 40°. It should be mentioned that the cut-in wind speed of the galloping energy harvester is proportional to the system damping and inversely proportional to the linear aerodynamic coefficient [63,76]. Therefore, an increase in the linear aerodynamic coefficient leads to a decrease in the cut-in wind speed, and a detailed discussion will be presented in Section 6.

4. Fully coupled model formulation

4.1. Energies in the system

The axial displacement of the beam can be expressed as follows:

$$u(x,z,t) = u(x,t) - z\frac{\partial w(x,t)}{\partial x} \tag{32}$$

where the $u(x, t)$ and $w(x, t)$ represent the axial displacement and transverse deflection, respectively, of the neutral layer at position x and time t. $u(x,z,t)$ represents the axial displacement at position (x,z) and time t. The motion of the tri-section beam is expressed by Equation (25). Employing the strain-deflection relations, the axial strain is derived as follows:

$$\varepsilon_{xx}(x,z,t) = \frac{\partial u(x,z,t)}{\partial x} = \frac{\partial u(x,t)}{\partial x} - z\frac{\partial^2 w(x,t)}{\partial x^2} \tag{33}$$

the stress of the substrate of the beam can be defined as:

$$\sigma_s = E_s\varepsilon_{xx}(x,z,t) = E_s\left(\frac{\partial u(x,t)}{\partial x} - z\frac{\partial^2 w(x,t)}{\partial x^2}\right) \tag{34}$$

where the E_s denotes Young's modulus of the substrate, and the stress-electric displacement form of the reduced constitutive equation for the piezoelectric transducer is expressed as:

$$\begin{Bmatrix} \sigma_1 \\ D_3 \end{Bmatrix} = \begin{bmatrix} \overline{c}_{11}^E & -\overline{e}_{31} \\ \overline{e}_{31} & \overline{\varepsilon}_{33}^s \end{bmatrix} \begin{bmatrix} \varepsilon_1 \\ E_3 \end{bmatrix} \tag{35}$$

where σ_1 and D_3 is the stress component and electric displacement component in the 1- and 3-directions (x- and z-directions) of the piezoelectric transducer, respectively. $\overline{c}_{11}^E$ is the elastic modulus of the piezoelectric layer at constant electric field, $\overline{e}_{31}$ and $\overline{\varepsilon}_{33}^S$ are the effective piezoelectric stress constant and permittivity constant, respectively. ε_1 is the strain of the piezoelectric transducer layer, E_3 is the electric field component, given the configuration with the parallel connection, the electric field component can be rearranged as $E_3 = -V(t)/d_{\mathrm{p}}$, where d_{p} is thickness of the piezoelectric transducer. Hence, the stress of the piezoelectric transducer layer can be defined as:

$$\sigma_1 = \overline{c}_{11}^E \varepsilon_1 - \overline{e}_{31} E_3 = \overline{c}_{11}^E \left(\frac{\partial u(x,t)}{\partial x} - z \frac{\partial^2 w(x,t)}{\partial x^2} \right) + \overline{e}_{31} \frac{V(t)}{d_{\mathrm{p}}} \tag{36}$$

the kinetic energy of the wind energy harvester can be written as follows:

$$\begin{aligned} T_{\mathrm{k}} &= \frac{1}{2} \left(\int_{V_{\mathrm{s}}} \rho_{\mathrm{s}} \frac{\partial \boldsymbol{u^t}}{\partial t} \frac{\partial \boldsymbol{u}}{\partial t} \mathrm{d}V_{\mathrm{s}} + \int_{V_{\mathrm{p}}} \rho_{\mathrm{p}} \frac{\partial \boldsymbol{u^t}}{\partial t} \frac{\partial \boldsymbol{u}}{\partial t} \mathrm{d}V_{\mathrm{p}} \right) + \frac{1}{2} M_{\mathrm{t}} \left[\left. \frac{\partial w(x,t)}{\partial t} \right|_{x=L_4} \right]^2 + \frac{1}{2} J_{\mathrm{t}} \left[\left. \frac{\partial^2 w(x,t)}{\partial x \partial t} \right|_{x=L_4} \right]^2 \\ &= \frac{1}{2} \left(\begin{array}{l} \displaystyle\int_{V_{\mathrm{s}}} \rho_{\mathrm{s}} \left\{ \left(\frac{\partial u(x,t)}{\partial t} - z \frac{\partial^2 w(x,t)}{\partial x \partial t} \right)^2 + \left(\frac{\partial w(x,t)}{\partial t} \right)^2 \right\} \mathrm{d}V_{\mathrm{s}} \\ \displaystyle + \int_{V_{\mathrm{p}}} \rho_{\mathrm{p}} \left\{ \left(\frac{\partial u(x,t)}{\partial t} - z \frac{\partial^2 w(x,t)}{\partial x \partial t} \right)^2 + \left(\frac{\partial w(x,t)}{\partial t} \right)^2 \right\} \mathrm{d}V_{\mathrm{p}} \end{array} \right) \\ &+ \frac{1}{2} M_{\mathrm{t}} \left[\left. \frac{\partial w(x,t)}{\partial t} \right|_{x=L_4} \right]^2 + \frac{1}{2} J_{\mathrm{t}} \left[\left. \frac{\partial^2 w(x,t)}{\partial x \partial t} \right|_{x=L_4} \right]^2 = \frac{1}{2} \sum_{r=1}^{N} \sum_{l=1}^{N} \left(\dot{q}_r(t) \dot{q}_l(t) \left(\sum m_{rl}^{aai} - 2 \sum m_{rl}^{abi} + \sum m_{rl}^{bbi} \right) \right) \end{aligned} \tag{37}$$

where ρ_{s} and ρ_{p} denote the densities of the substrate beam and piezoelectric transducer. M_{t} and I_{t} denote the tip mass and moment of inertia of the bluff body, respectively, and the integrations are performed over the volumes (V_{s} and V_{p}) of the substrate beam and piezoelectric transducer. The related general mass parameters can be rearranged as follows:

$$m_{rl}^{aai} = \sum_{i=1}^{4} \int_{L_i} I_1^{T(i)} \phi_r(x) \phi_l(x) dx + M_{\mathrm{t}} \phi_r(L_4) \phi_l(L_4) + J_{\mathrm{t}} \phi_r'(L_4) \phi_l'(L_4) \tag{38}$$

$$m_{rl}^{abi} = \int_{L_i} I_2^{T(i)} \phi_r'(x) \psi_l(x) dx m_{rl}^{bbi} = \int_{L_i} I_1^{T(i)} \psi_r(x) \psi_l(x) dx \tag{39}$$

the potential energy of the wind energy harvester can be written as follows:

$$\begin{aligned} U_{\mathrm{p}} &= \frac{1}{2} \left(\int_{V_{\mathrm{s}}} \varepsilon_{xx} \sigma_{\mathrm{s}} dV_{\mathrm{s}} + \int_{V_{\mathrm{p}}} \varepsilon_{xx} \sigma_1 dV_{\mathrm{p}} \right) = \frac{1}{2} \int_{V_{\mathrm{s}}} E_{\mathrm{s}} \left(\frac{\partial u(x,t)}{\partial x} - z \frac{\partial^2 w(x,t)}{\partial x^2} \right)^2 dV_{\mathrm{s}} \\ &+ \frac{1}{2} \int_{V_{\mathrm{p}}} \overline{c}_{11}^E \left(\frac{\partial u(x,t)}{\partial x} - z \frac{\partial^2 w(x,t)}{\partial x^2} \right)^2 dV_{\mathrm{p}} + \frac{1}{2} \int_{V_{\mathrm{p}}} \overline{e}_{31} \frac{v(t)}{h_{\mathrm{p}}} \left(\frac{\partial u(x,t)}{\partial x} - z \frac{\partial^2 w(x,t)}{\partial x^2} \right) dV_{\mathrm{p}} \\ &= \frac{1}{2} \sum_{r=1}^{N} \sum_{l=1}^{N} \left(q_r(t) q_l(t) \left(\sum k_{rl}^{aai} - 2 \sum k_{rl}^{abi} + \sum k_{rl}^{bbi} \right) \right) + \frac{1}{2} \sum_{r=1}^{N} q_r(t) V(t) \left(\widetilde{\chi}_r^b - \widetilde{\chi}_r^a \right) \end{aligned} \tag{40}$$

where σ_{s} and σ_1 denote the stress of the substrate beam and piezoelectric transducers. The related general stiffness parameters of the kinetic energy can be rearranged follow:

$$k_{rl}^{aai} = \int_{L_i} I_3^{U(i)} \phi_r''(x) \phi_l''(x) dx k_{rl}^{abi} = \int_{L_i} I_2^{U(i)} \phi_r''(x) \psi_l'(x) dx k_{rl}^{bbi} = \int_{L_i} I_1^{U(i)} \psi_r'(x) \psi_l'(x) dx \tag{41}$$

the internal electrical energy of the wind energy harvester can be written as follows:

$$\begin{aligned} W_{\mathrm{ie}} &= \frac{1}{2} \int_{V_{\mathrm{p}}} \boldsymbol{E}_3 \boldsymbol{D} \mathrm{d}V_{\mathrm{p}} = \frac{1}{2} \int_{V_{\mathrm{p}}} \frac{-V(t)}{d_{\mathrm{p}}} \left(\overline{e}_{31} \varepsilon_1 + \overline{\varepsilon}_{33}^S \frac{-V(t)}{d_{\mathrm{p}}} \right) \mathrm{d}V_{\mathrm{p}} = -\frac{1}{2} \int_{V_{\mathrm{p}}} \frac{V(t)}{d_{\mathrm{p}}} \left(\overline{e}_{31} \left(\frac{\partial u(x,t)}{\partial x} - z \frac{\partial^2 w(x,t)}{\partial x^2} \right) - \overline{\varepsilon}_{33}^S \frac{V(t)}{d_{\mathrm{p}}} \right) \mathrm{d}V_{\mathrm{p}} \\ &= \frac{1}{2} V(t) q_r(t) \int_0^{L_1} \left[\left(J_{\mathrm{p}} \sum_{r=1}^{N} \phi_r''(x) \right) - \left(B_{\mathrm{p}} \sum_{r=1}^{N} \psi_r'(x) \right) \right] dx + \frac{1}{2} C_{\mathrm{p}} V^2(t) = \frac{1}{2} \sum_{r=1}^{N} q_r(t) V(t) \left(\widetilde{\chi}_r^a - \widetilde{\chi}_r^b \right) + \frac{1}{2} C_{\mathrm{p}} V^2(t) \end{aligned} \tag{42}$$

where C_p is the internal capacitance of the piezoelectric transducer, $\tilde{\chi}^\mathrm{a}_\mathrm{r} - \tilde{\chi}^\mathrm{b}_\mathrm{r}$ is the modal electromechanical coupling term. The expressions for these terms are:

$$C_\mathrm{p} = \iint_{A_\mathrm{p}} \frac{\bar{\varepsilon}^S_{33}}{d_\mathrm{p}} dydz \tilde{\chi}^a_r = \int_{L_1} J_\mathrm{p} \phi''_r(x) dx \tilde{\chi}^b_r = \int_{L_1} B_\mathrm{p} \psi'_r(x) dx \tag{43}$$

where

$$J_\mathrm{p} = \iint_{A_\mathrm{p}} z \frac{\bar{e}_{31}}{d_\mathrm{p}} dydz, B_\mathrm{p} = \iint_{A_\mathrm{p}} \frac{\bar{e}_{31}}{d_\mathrm{p}} dydz \tag{44}$$

The related parameters of Equations (38), (39) and (41) are given as follows:

$$\begin{bmatrix} \iint_{A_{\mathrm{s}_1}} dydz & \iint_{A_\mathrm{p}} dydz \\ \iint_{A_{\mathrm{s}_1}} zdydz & \iint_{A_\mathrm{p}} zdydz \\ \iint_{A_{\mathrm{s}_1}} z^2 dydz & \iint_{A_\mathrm{p}} z^2 dydz \end{bmatrix} \begin{bmatrix} \rho_\mathrm{s} \\ \rho_\mathrm{p} \end{bmatrix} = \begin{bmatrix} I_1^{T(1)} \\ I_2^{T(1)} \\ I_3^{T(1)} \end{bmatrix} \quad \begin{bmatrix} \iint_{A_{\mathrm{s}_\mathrm{j}}} dydz & \iint_{A_\mathrm{p}} dydz \\ \iint_{A_{\mathrm{s}_\mathrm{j}}} zdydz & \iint_{A_\mathrm{p}} zdydz \\ \iint_{A_{\mathrm{s}_\mathrm{j}}} z^2 dydz & \iint_{A_\mathrm{p}} z^2 dydz \end{bmatrix} \begin{bmatrix} \rho_\mathrm{s} \\ 0 \end{bmatrix} = \begin{bmatrix} I_1^{T(j)} \\ I_2^{T(j)} \\ I_3^{T(j)} \end{bmatrix} (j = 2, 3, 4) \tag{45}$$

$$\begin{bmatrix} \iint_{A_{\mathrm{s}_1}} dydz & \iint_{A_\mathrm{p}} dydz \\ \iint_{A_{\mathrm{s}_1}} zdydz & \iint_{A_\mathrm{p}} zdydz \\ \iint_{A_{\mathrm{s}_1}} z^2 dydz & \iint_{A_\mathrm{p}} z^2 dydz \end{bmatrix} \begin{bmatrix} Y_\mathrm{s} \\ \bar{c}^E_{11} \end{bmatrix} = \begin{bmatrix} I_1^{U(1)} \\ I_2^{U(1)} \\ I_3^{U(1)} \end{bmatrix} \quad \begin{bmatrix} \iint_{A_{\mathrm{s}_\mathrm{j}}} dydz & \iint_{A_\mathrm{p}} dydz \\ \iint_{A_{\mathrm{s}_\mathrm{j}}} zdydz & \iint_{A_\mathrm{p}} zdydz \\ \iint_{A_{\mathrm{s}_\mathrm{j}}} z^2 dydz & \iint_{A_\mathrm{p}} z^2 dydz \end{bmatrix} \begin{bmatrix} Y_\mathrm{s} \\ 0 \end{bmatrix} = \begin{bmatrix} I_1^{U(j)} \\ I_2^{U(j)} \\ I_3^{U(j)} \end{bmatrix} (j = 2, 3, 4) \tag{46}$$

The non-conservative virtual work of the wind energy harvester can be written as follows:

$$W_\mathrm{nc} = Q(t)V(t) + F_g \left(\sum_{r=1}^{N} q_r(t) \phi_{4r}(L_4) \cos\theta + \sum_{r=1}^{N} q_r(t) \psi_{4r}(L_4) \sin\theta \right) \tag{47}$$

where $Q(t)$ is the electric charge output of the piezoelectric transducer and F_g denotes the transverse aerodynamic force.

4.2. Aero-Electro-Mechanical governing equations

The aero-electro-mechanical coupling equations can be derived by using the Lagrange's Equations

$$\frac{\mathrm{d}}{\mathrm{d}t} \left(\frac{\partial T_\mathrm{k}}{\partial \dot{q}_\mathrm{k}} \right) - \frac{\partial T_\mathrm{k}}{\partial q_\mathrm{k}} + \frac{\partial U_\mathrm{p}}{\partial q_\mathrm{k}} - \frac{\partial W_\mathrm{ie}}{\partial q_\mathrm{k}} - \frac{\partial W_\mathrm{nc}}{\partial q_\mathrm{k}} = 0 \tag{48}$$

and substituting Equations (37), (40), (42) and (47) into (49), the fully coupled aero-electro-mechanical governing equations of the system can be obtained as

$$\begin{aligned} \sum_{r=1}^{N} \ddot{q}_r(t) \left(\sum_{i=1}^{4} m^{aai}_{kr} - 2 \sum_{i=1}^{4} m^{abi}_{kr} + \sum_{i=1}^{4} m^{bbi}_{kr} \right) + \sum_{r=1}^{N} q_r(t) \left(\sum_{i=1}^{4} k^{aai}_{kr} - 2 \sum_{i=1}^{4} k^{abi}_{kr} + \sum_{i=1}^{4} k^{bbi}_{kr} \right) \\ + V(t) \left(\tilde{\chi}^b_k - \tilde{\chi}^a_k \right) = F_g (\phi_{4k}(L_4) \cos\theta + \psi_{4k}(L_4) \sin\theta) \end{aligned} \tag{49}$$

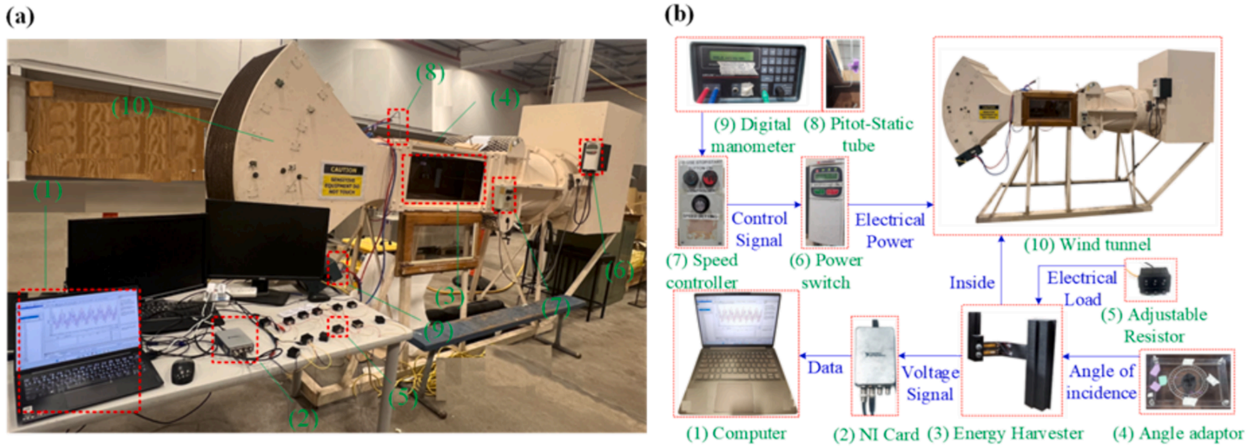

Fig. 6. Prototype of the proposed multi-directional galloping-based energy harvester and experimental setup for wind tunnel test: (a) experimental setup and (b) control and data flow chart.

$$\frac{V(t)}{R_L}+C_p\dot{V}(t)-\sum_{r=1}^{N}\dot{q}_r(t)\left(\tilde{\chi}_r^b-\tilde{\chi}_r^a\right)=0 \tag{50}$$

where the transverse aerodynamic force of galloping of the energy harvester is

$$F_g=\frac{1}{2}\rho hlU^2C_{Fy}=\frac{1}{2}\rho hlU^2\left[C_1\delta+C_3\delta^3+C_5\delta^5\right] \tag{51}$$

where ρ denotes the air density, the h, l are height and length of the bluff body, U is the incident wind speed, C_{Fy} denotes the transverse galloping coefficient, C_1, C_3 and C_5 are the empirical aerodynamic coefficients of polynomial expansion, which are obtained through the CFD simulation in Section 3. The δ represents the wind angle of attack:

$$\delta=\frac{\sum_{r=1}^{N}\dot{q}_r(t)(\phi_{4r}(L_4)\cos\theta+\psi_{4r}(L_4)\sin\theta)}{U}+\sum_{r=1}^{N}q_r(t)\phi'_{4r}(L_4) \tag{52}$$

Considering the coupled first and second order bending modes, and substituting the Rayleigh damping into the system, Equations (49) and (50) become

$$\begin{cases}\widetilde{M}_1\ddot{q}_1(t)+\widetilde{C}_1\dot{q}_1(t)+\widetilde{K}_1q_1(t)+\widetilde{\lambda}_1V(t)=\widetilde{F}_1\\ \widetilde{M}_2\ddot{q}_2(t)+\widetilde{C}_2\dot{q}_2(t)+\widetilde{K}_2q_2(t)+\widetilde{\lambda}_2V(t)=\widetilde{F}_2\\ V(t)/_{R_L}+C_p\dot{V}(t)-\left(\widetilde{\lambda}_1\dot{q}_1(t)+\widetilde{\lambda}_2\dot{q}_2(t)\right)=0\end{cases} \tag{53}$$

Here, $\widetilde{M}_1$, $\widetilde{M}_2$, $\widetilde{C}_1$, $\widetilde{C}_2$, $\widetilde{K}_1$, $\widetilde{K}_2$, $\widetilde{\lambda}_1$, $\widetilde{\lambda}_2$, $\widetilde{F}_1$ and $\widetilde{F}_2$ represent the modal mass, modal damping, modal stiffness, modal electromechanical coupling term, and modal mechanical forcing function of the first- and second order bending mode respectively (see Appendix C for related parameters). Equations (53) can be rearranged into the state vector form as:

$$\boldsymbol{X}=\begin{Bmatrix}X_1\\X_2\\X_3\\X_4\\X_5\end{Bmatrix}=\begin{Bmatrix}q_1\\\dot{q}_1\\q_2\\\dot{q}_2\\V\end{Bmatrix} \tag{54}$$

The governing equations then can be rearranged in the state space form.

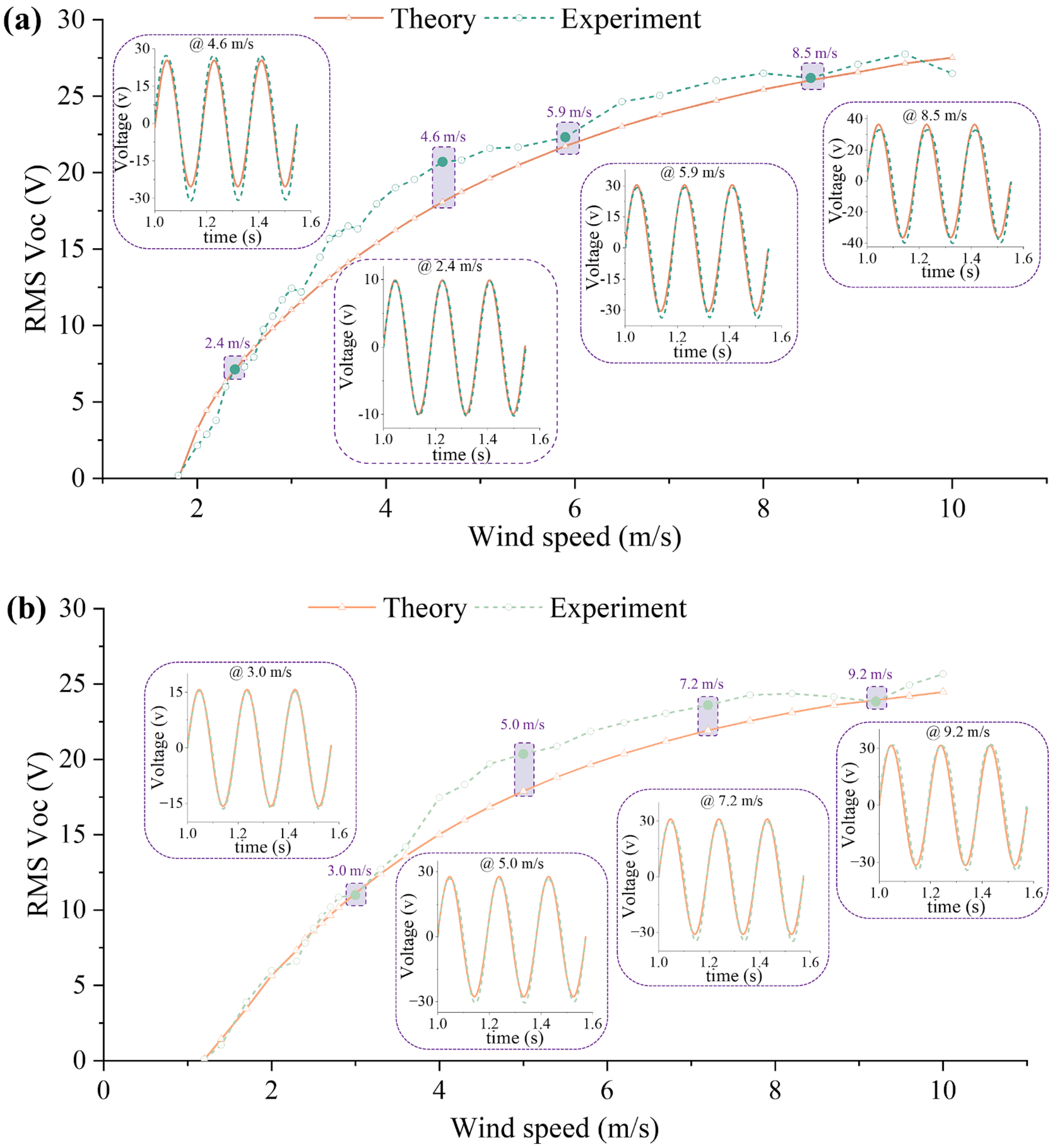

Fig. 7. Comparison of RMS V_{OC} from theoretical model and experiment with the harvester in the first order bending mode subjected to wind flows from incident directions of (a) −49° and (b) −45.

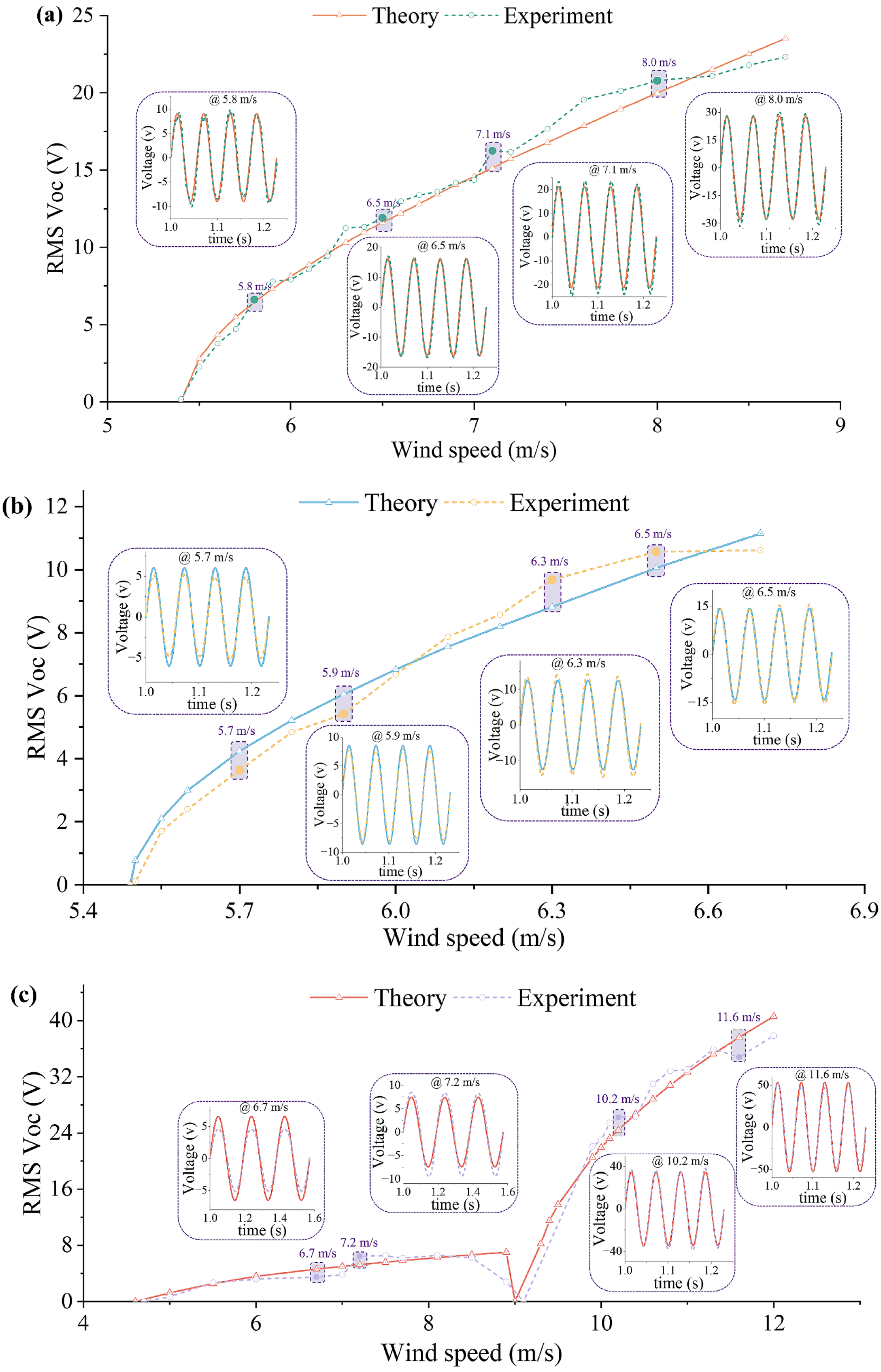

(caption on next page)

Fig. 8. Comparison of RMS V_{OC} from theoretical model and experiment with the harvester galloping in the second order bending mode or with mode transition subjected to wind flows from incident directions of (a) 40° and (b) 43° (second order bending mode), and (c) 35° (first order to second order bending mode transition).

$$\dot{\boldsymbol{X}} = \begin{Bmatrix} \dot{q}_1 \\ \ddot{q}_1 \\ \dot{q}_2 \\ \ddot{q}_2 \\ \dot{V} \end{Bmatrix} = \begin{Bmatrix} X_2 \\ \dfrac{\widetilde{F}_1}{\widetilde{M}_1} - \dfrac{\widetilde{C}_1}{\widetilde{M}_1}X_2 - \dfrac{\widetilde{K}_1}{\widetilde{M}_1}X_1 - \dfrac{\widetilde{\lambda}_1}{\widetilde{M}_1}X_5 \\ X_4 \\ \dfrac{\widetilde{F}_2}{\widetilde{M}_2} - \dfrac{\widetilde{C}_2}{\widetilde{M}_2}X_4 - \dfrac{\widetilde{K}_2}{\widetilde{M}_2}X_3 - \dfrac{\widetilde{\lambda}_2}{\widetilde{M}_2}X_5 \\ \dfrac{\widetilde{\lambda}_1 X_2 + \widetilde{\lambda}_2 X_4}{C_p} - \dfrac{X_5}{R_L C_p} \end{Bmatrix} \tag{55}$$

The response of the proposed galloping-based piezoelectric energy harvester can be obtained by employing numerical tools, such as ODE45 in MATLAB, and the detailed result discussion is presented in Section 6.

5. Experiment

Fig. 6 shows the prototyped galloping-based energy harvester and the experimental setup for wind tunnel test. The harvester (item (3)) comprises a tri-section beam bonded with MFCs, a square cross-sectional bluff body with splitters, and a harvester holder. The tri-section beam, and the bluff body were 3D-printed using Polylactic Acid (PLA). The harvester holder was utilized to clamp the harvester beam and position the harvester at an appropriate location in the wind tunnel. An angle adapter (item (4)) and its corresponding scale were fabricated using laser cutting to monitor the incident wind direction. Aerodynamic testing was conducted in an open-loop wind tunnel (item (10)). The incoming wind flow was generated by a draft fan. A pitot-static tube (item (8)) was employed to measure the real-time wind speed, which was displayed on a digital manometer (item (9)), and a speed controller (item (7)) was utilized to regulate the incident wind speed. The direction of the wind flow incident on the harvester was adjusted using the angle adapter, which was positioned at the top of the wind tunnel's test section. A data acquisition (DAQ, item (2)) module (NI 9229, National Instruments) was employed to acquire and process the electrical signal on a computer (item (1)).

6. Results and discussion

6.1. Model validation

To validate the model derived in Section 4, the open circuit voltages (V_{OC}) from the model are compared with the experimental results of the harvester with different wind speeds and directions. For the electrical output measurement, the open circuit voltage and the power output across the load resistance (R_L) are of concern [70]. The internal impedance of the piezoelectric transducer ($\approx 1/(2\pi f C_{\mathrm{p}})$) varies with different galloping frequencies. For instance, in the first order bending mode with the frequency of 5.24 Hz in the experiment, the internal impedance of the piezoelectric transducer with a capacitance (C_{p}) of 15 nF is 2.02 MΩ. Similarly, in the second order bending mode with the frequency of 17.35 Hz, the internal impedance of the energy harvester is 0.61 MΩ.

Fig. 7 shows the results for the harvester excited to gallop in the first bending mode with the wind flow from incident directions of -45° and -49°. It can be observed that the root-mean-square (RMS) voltages obtained from the theoretical model and experiment generally show the consistent results and the increasing trend of the voltage output with the increase of wind speed. Fig. 7(a) and (b) also show the detailed time-domain voltage waveforms at different wind speeds for varying incident wind direction (2.4 m/s, 4.6 m/s, 5.9 m/s, and 8.5 m/s for the incident wind direction of -49°; 3.0 m/s, 5.0 m/s, 7.2 m/s, and 9.2 m/s for the incident wind direction of -45°). Again, the theoretical model exhibits good agreement with the experimental results. From Fig. 7(a) and (b), it is noted that the critical wind speeds (referred to as cut-in wind speed U_{cr}) of galloping for the incident wind directions of -49° and -45° are 1.8 m/s and 1.2 m/s, respectively. It is noteworthy that when the incident wind direction is -49°, the simulated linear aerodynamic coefficient C_1 has a lower value of 2.183, compared to 2.871 for -45°. These values of cut-in wind speeds corroborate the conclusion elucidated in Section 3 that a lower linear aerodynamic coefficient corresponds to a higher cut-in wind speed in one vibrational mode.

Fig. 8(a) and (b) show the results for the harvester excited to gallop in the second bending mode with the wind flow from incident directions of 40° and 43°. Again, the theoretical results derived from the model agree well with the experimental results. In Fig. 8(a) and (b), the time-domain voltage waveforms at four different wind speeds (5.8 m/s, 6.5 m/s, 7.1 m/s, and 8.0 m/s) are chosen to compare against experiment when the incident wind direction is 40°, and the time-domain voltage waveforms at another four various wind speeds (5.7 m/s, 5.9 m/s, 6.3 m/s, and 6.5 m/s) are chosen to compare against experiment for the incident wind direction of 43°. The cut-in wind speed varies with different incident wind directions, measuring 5.4 m/s at the incident wind direction of 40° compared to 5.5 m/s at 43°. This also corroborates the conclusion in Section 3 that a higher linear aerodynamic coefficient ($C_1 = 3.108$ at 40° and $C_1 = 2.926$ at 43°) corresponds to a lower cut-in wind speed in the same vibration mode.

Fig. 8(c) shows one case that the harvester gallops with the mode transition from the first order bending mode to the second order

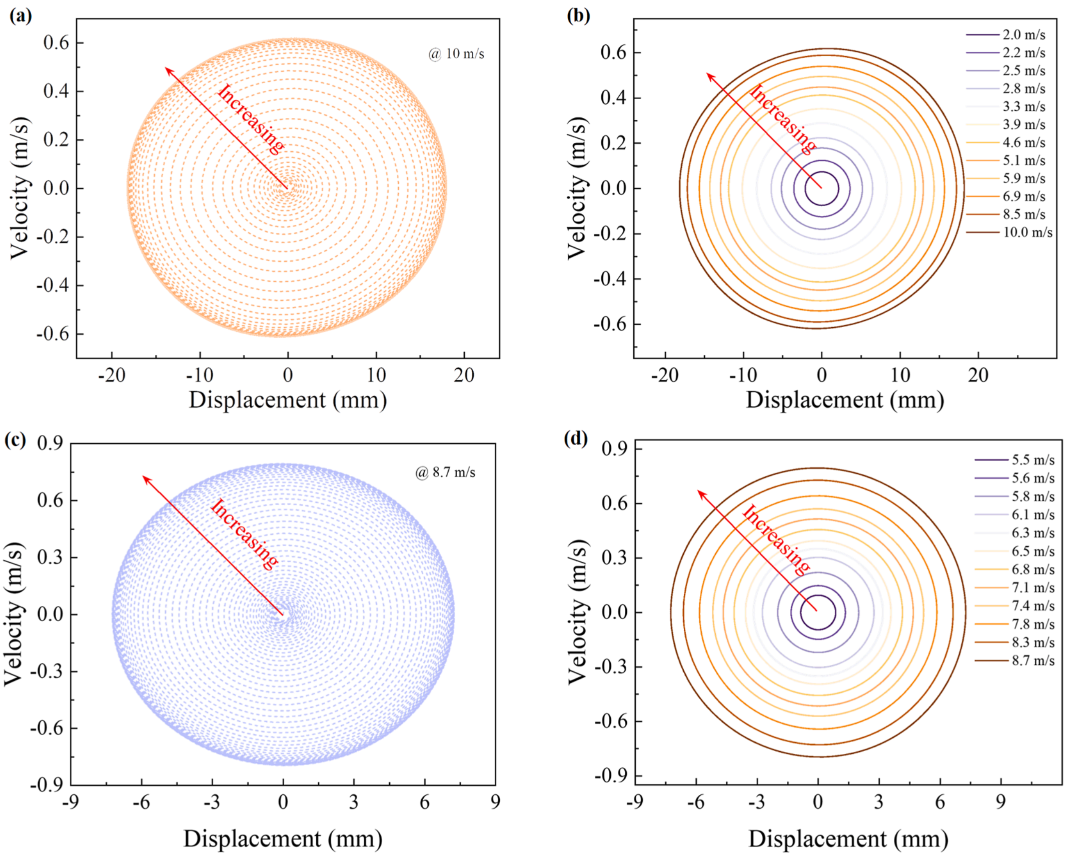

Fig. 9. Limit cycle oscillations and phase portraits of the harvester when galloping in the first and second order bending modes. (a) Progressing to limit cycle at wind speed of 10.0 m/s and (b) limit cycles at different wind speeds for the first order bending mode at an incident wind direction of −49°; (c) Progressing to limit cycle at wind speed of 8.7 m/s and (d) limit cycles at different wind speeds for the second order bending mode at an incident wind direction of 40°.

bending mode with the increase of wind speed. In Fig. 8(c), the time-domain voltage waveforms at four different wind speeds (6.7 m/s, 7.2 m/s, 10.2 m/s, and 11.6 m/s) are chosen to compare against experiment when the incident wind direction is 35°. It is noteworthy that when the linear aerodynamic coefficient remains the same for the incident wind direction of 35°, the cut-in wind speed for the second order bending mode is higher than that for the first order bending mode, due to the higher mechanical damping associated with the second order bending mode. Different cut-in wind speeds can be observed under varying wind direction when the first order bending mode is triggered, measuring 4.7 m/s at an incident wind direction of 35°, higher than those at −49° (1.8 m/s) and at −45° (1.2 m/s). Again, this corroborates the conclusion in Section 3 that a higher linear aerodynamic coefficient ($C_1 = 1.871$ at 35°, $C_1 = 2.183$ at −49°, and $C_1 = 2.871$ at −45°) corresponds to a lower cut-in wind speed within the same vibration mode.

6.2. *Limit cycle oscillation*

The input aerodynamic force can be regarded as an effective nonlinear damping component of the harvester system, rendering the galloping motions to be apparently "self-excited". From the theoretical perspective, the linear and nonlinear coefficients of the overall damping [77] can then be expressed as:

$$D - 0.5\rho hlUC_1 \quad \text{linear} \tag{56}$$

$$-0.5\rho hlU\left[\sum\nolimits_{i=2,\dots} C_{2i-1}\left(\dot{w}(t)/U\right)^{i-1}\right] \quad \text{nonlinear.} \tag{57}$$

It is noteworthy that for a low wind speed U, the nonlinear term can be neglected, and the system is governed by the positive linear damping, resulting in the system being damped to the equilibrium state. However, as U increases, the linear damping becomes negative beyond the cut-in wind speed U_{cr}. Consequently, the system loses the aerodynamic stability, and the vibration amplitude increases. Nonetheless, the higher-order nonlinear damping terms simultaneously limit the amplitude, leading to the damping back to zero and progressing to the limit cycle oscillations.

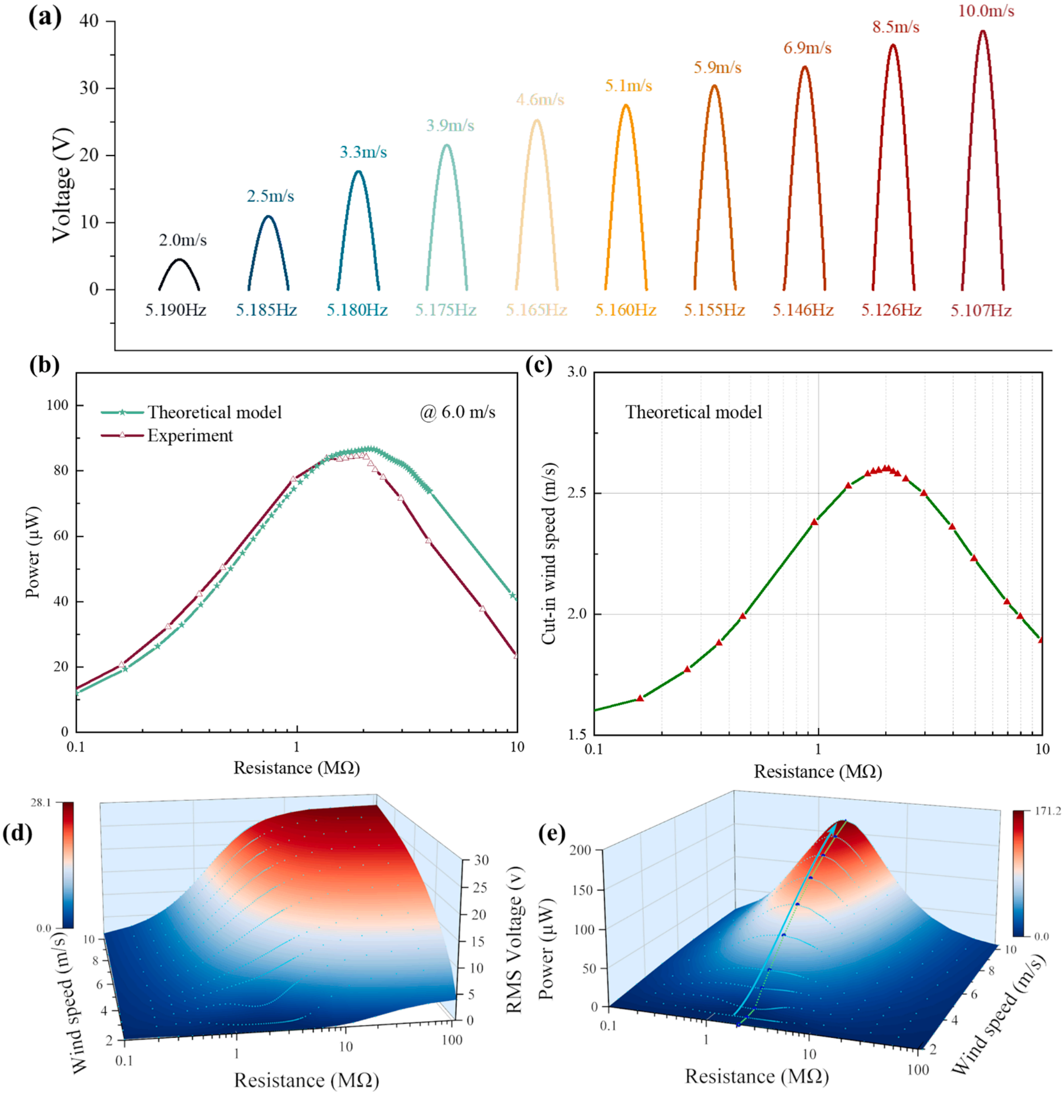

Fig. 10. Predicted performance of the proposed galloping-based energy harvester in the first order bending mode at the wind direction of −49° from the theoretical model: (a) oscillation frequency and voltage output amplitude for varying wind speeds, (b) power output with varying resistance at the wind speed of 6 m/s with comparison to the wind tunnel test results, (c) cut-in wind speed with varying resistive load, (d) RMS voltage and (e) average power output with varying resistive load and wind speed.

Fig. 9 elucidates the limit cycle oscillation and phase portrait when the harvester gallops in the first order and second order bending modes at different incident wind speeds and directions. When the incident wind direction and speed are −49° and 10.0 m/s, as shown in Fig. 9(a), the energy harvester undergoes the first order bending mode, and the vibration displacement and velocity exhibit a steady increase from zero to the final steady state. The size of the limit oscillation cycle also increases with the increasing wind speed from 2.0 m/s to 10.0 m/s, as illustrated in Fig. 9(b). This increasing trend can be observed when the harvester undergoes the second order bending vibration with the incident wind direction of 40° and the wind speed of 8.7 m/s, and the size of the phase portrait also increases as the wind speed rising from 5.5 m/s to 8.7 m/s, as illustrated in Fig. 9(c) and (d).

6.3. Output performance

Fig. 10(a) illustrates the influence of wind speed U on the first order bending oscillation frequency of the harvester with the incident wind direction of −49°. Firstly, the oscillation frequency (5.19 Hz with open circuit) of galloping from simulation is slightly larger than the fundamental natural frequency (5.14 Hz) of the harvester. As depicted in Fig. 10(a), the oscillation frequency is slightly affected by U, and it declines with the increasing wind speed U from 2.0 m/s to 10.0 m/s. This phenomenon can be attributed to the change in the rotation angle at the free end of the cantilever with varying wind speed U. Similar observations can be found in some previously published results [68,77]. As illustrated in Fig. 10(b), for a representative wind speed of 6.0 m/s, the peak power output is achieved

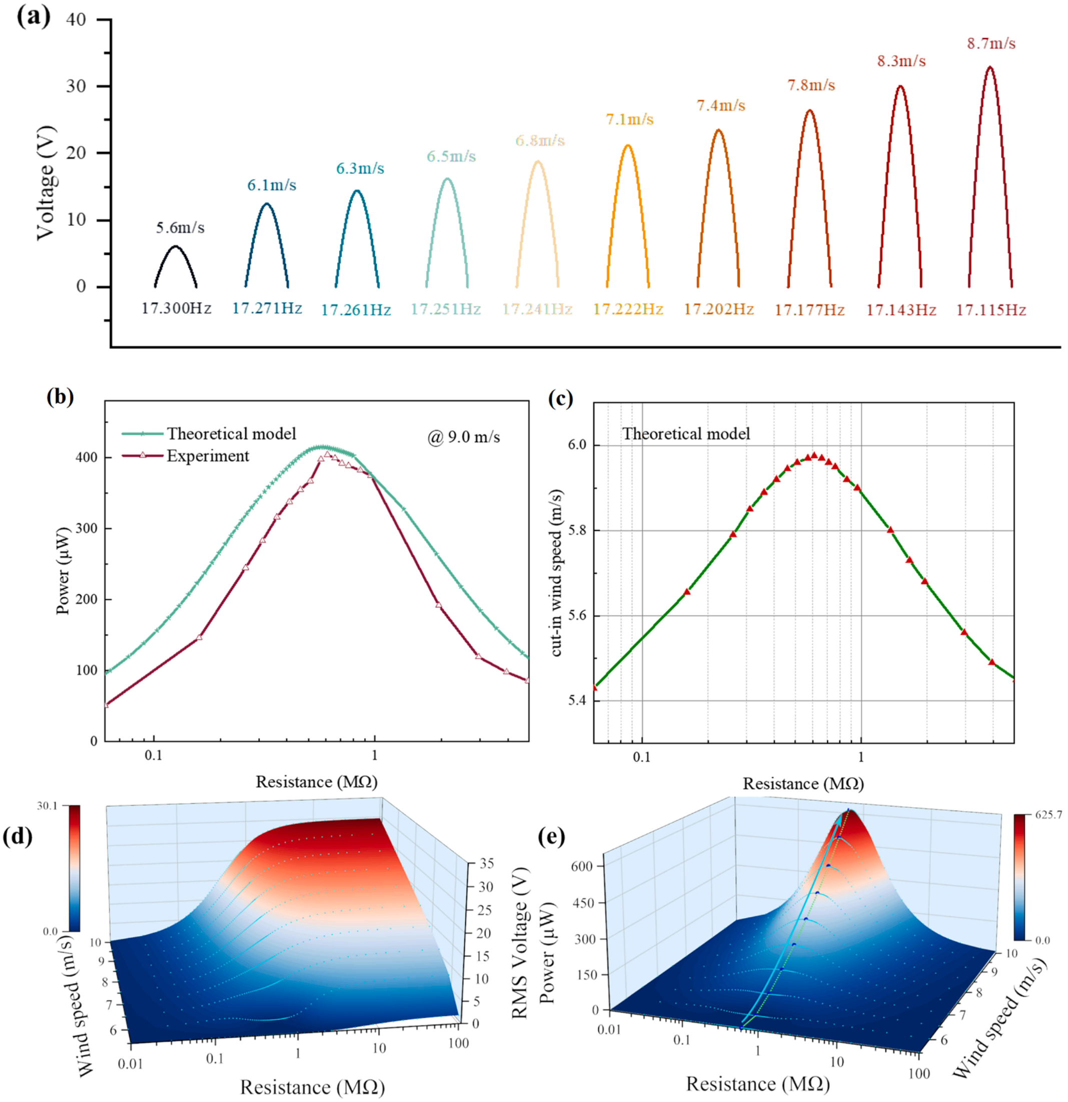

Fig. 11. Predicted performance of the proposed galloping-based energy harvester in the second order bending mode at the wind direction of 40° from the theoretical model: (a) oscillation frequency and voltage output amplitude for varying wind speeds, (b) power output with varying resistance at the wind speed of 9 m/s with comparison to the wind tunnel test results, (c) cut-in wind speed with varying resistive load, (d) RMS voltage and (e) average power output with varying resistive load and wind speed.

when the load resistance is close to the internal impedance of 2.06 MΩ of the harvester in the first order bending mode and the results from theoretical model and wind tunnel experiment are generally consistent. In addition, a detailed analysis of the variation of the cut-in wind speed with the load resistance is illustrated in Fig. 10(c). It is noted that galloping is more likely to be triggered at lower cut-in wind speeds in short-circuit and open-circuit conditions. However, when the load resistance approaches the internal impedance of the harvester, the onset of galloping is suppressed with a higher cut-in wind speed.

Fig. 10(d) and (e) interpret the overall performance of the harvester at different wind speeds and resistance loads in terms of RMS voltage and average power output. A shallow valley is also observed in Fig. 10(d) for lower wind speed ranges (below 3.0 m/s) around the matched load resistance of 2.06 MΩ. When the incident wind speed exceeds 3.0 m/s, the RMS voltage increases monotonically increases with the load resistance until saturation (open-circuit condition). In Fig. 10(e), it is observed that around the matched load resistance 2.06 MΩ, there exists either a valley or a peak for a specific incident wind speed. When the incident wind speed is less than 2.0 m/s, there is no power output for the resistance loads between the range of 0.4 MΩ to 7.0 MΩ, as the cut-in wind speed between these resistance loads range are larger than 2.0 m/s due to the electrical damping effect. When the wind speed is $U = 3.0$ m/s, which is just larger than the cut-in wind speed (2.60 m/s) under the resistance loads of 2.06 MΩ, a shallow valley is formed. This is due to the fact that a maximum electrical damping occurs at the matched load resistance compared to the load resistances away from the matched load resistance. This leads to a significantly increased cut-in wind speed at the matched load resistance. Therefore, when the wind

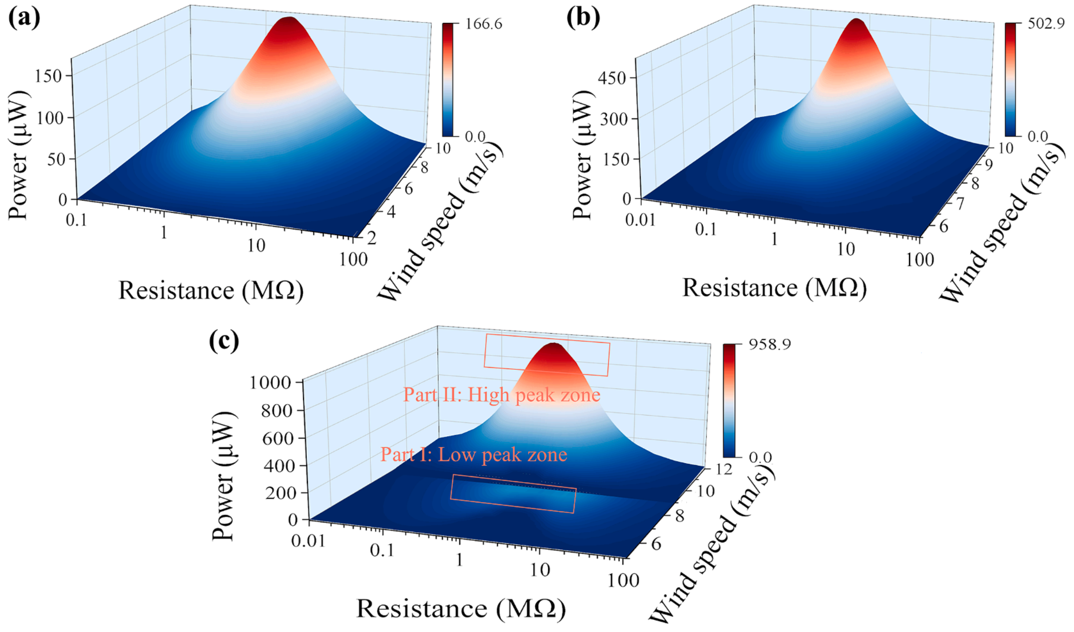

Fig. 12. Predicted power output performance of the proposed galloping-based energy harvester in different bending modes at other incident wind directions: (a) first order bending mode at −45°, (b) second order bending mode at 43°, and (c) first order to second order bending mode transition at 35°.

speed slightly exceeds the cut-in wind speed at the optimal load resistance, the output is still much lower than the outputs at other resistances with much lower cut-in wind speeds, thereby forming a shallow valley around the matched load resistance. Similar observations have been reported in previously published study [77]. Further increasing the wind speed, the valley changes to a peak and reaches an average power of 171.2 μW at the wind speed of 10 m/s.

Fig. 11(a) illustrates the influence of wind speed U on the second order bending oscillation frequency of the harvester with the incident wind direction of 40°. Firstly, the simulation oscillation frequency (17.30 Hz with open circuit) of galloping from simulation is lightly larger than the fundamental natural frequency (17.25 Hz) of the harvester. Similar to the galloping in the first order bending mode, the oscillation frequency in the second order bending mode is slightly affected by U, and it declines with the increasing wind speed U from 5.6 m/s to 8.7 m/s. As illustrated in Fig. 11(b), for a representative wind speed of 9.0 m/s, the peak power output is achieved when the load resistance is close to the internal impedance of 0.615 MΩ of the harvester in the second order bending mode and the results from theoretical model and wind tunnel experiment are generally consistent. In addition, a detailed analysis of the variation of the cut-in wind speed with the load resistance is illustrated in Fig. 11(c). The galloping is also more likely to be triggered at lower cut-in wind speeds in short-circuit and open-circuit conditions in the second order bending mode. When the load resistance approaches the internal impedance of the harvester, the onset of galloping is suppressed with a higher cut-in wind speed.

Fig. 11(d) and (e) elucidate the overall performance of the harvester at different wind speeds and resistance loads in terms of RMS voltage and average power output. Similar to the galloping in the first order bending mode, a shallow valley is also observed in Fig. 11 (d) for lower wind speed ranges (below 6.0 m/s) around the matched load resistance of 0.615 MΩ. When the incident wind speed exceeds 6.0 m/s, the RMS voltage increases monotonically increases with the load resistance until saturation (open-circuit condition). In Fig. 11(e), it is observed that around the matched load resistance 0.615 MΩ, there exists either a valley or a peak for a specific incident wind speed. When the incident wind speed is less than 5.5 m/s, there is no power output for the resistance loads between the range of 0.08 MΩ to 4.0 MΩ, since the cut-in wind speed between these resistance loads range are larger than 5.5 m/s. When the wind speed is $U = 6.0$ m/s, which is just larger than the cut-in wind speed (5.97 m/s) under the resistance loads of 0.615 MΩ, a shallow valley is formed due to maximum electrical damping occurring at the matched load resistance. Further increasing the wind speed, the valley changes to a peak and reaches an average power of 625.7 μW at the wind speed of 10 m/s. Furthermore, it is worth noting that the harvester galloping in the higher bending mode possesses superior power output compared to that in the first order bending mode mainly due to similar voltage output but much lower matched load resistance at a higher oscillation frequency.

The power output performance in other incident wind directions ($\theta = 43°$, $-45°$, and 35°) is also presented in Fig. 12. The harvester achieves a superior power output at 502.9 μW while undergoing the second order bending mode with an incident wind direction of 43°, compared to a power output of 166.6 μW obtained from the first order bending mode with an incident wind direction of −45°. This further confirms that the harvester galloping in the second order bending mode is preferred over the first order bending mode for harnessing wind energy. When the incident wind direction is 35°, the vibrational mode will experience a mode transition in this wind speed range. To be specified, the harvester will trigger the first order bending mode within the smaller wind speed range of 5.0 m/s to 9.0 m/s, and when the wind speed exceeds 9.0 m/s, the second order bending mode will be triggered. As depicted in Fig. 12(c), within the lower wind range (between 5.0 m/s and 9.0 m/s), the output power of the harvester galloping in the first order bending mode increases to a lower peak (part I zone), and then drops to zero at 9.0 m/s. When the galloping is transitioned to the second order bending mode, the output power of the harvester increases to a higher peak (part II zone) and achieves 958.9 μW at $U = 12$ m/s.

7. Conclusions

Through comprehensive theoretical modeling, this work investigated the multi-modal behavior of the galloping energy harvester with a tri-section beam subjected to different incident wind directions. A fully coupled aero-electro-mechanical model is established with the modal properties obtained by global mode method (GMM) and validated by the finite element method (FEM), and transverse aerodynamic force coefficients of the bluff body in different incident wind directions obtained by computational fluid dynamics (CFD). Wind tunnel tests validate the theoretical model in terms of electrical output performance and cut-in wind speeds in different triggered modes. The main conclusions from this work are as follows.

- A novel coupled modeling approach has been established and validated for galloping energy harvesters, which provides the theoretical foundation for the design of such harvesters with complex beam structures and bluff bodies for improving energy harvesting performance.
- The proposed galloping energy harvester with tri-section beam can harness wind energy from multiple directions with multiple modes capable of being triggered.
- Much higher electric outputs can be achieved by the proposed harvester when galloping is triggered in the second order bending mode compared to the first order bending mode, though with a higher cut-in wind speed.
- At a specific incident wind direction (35°), mode transition is predicted by the model and observed in the experiment in the entire wind speed range, with the harvester being triggered in the first order bending mode in the wind speed range of 5.0 m/s to 9.0 m/s and in the second order bending mode above 9.0 m/s.

This technology provides theoretical insights into the multi-modal galloping behavior and offers a solution for continuous power source for sensor networks and low-power electronic devices, particularly in remote or inaccessible areas, enabling the monitoring of environmental conditions, infrastructure, and natural disasters. Although the developed harvester enables multi-directional wind energy harvesting, the relatively high cut-in wind speed required to trigger the second order bending mode remains a challenge. Further research is required to lower the cut-in wind speed of higher bending modes, thereby enabling more effective wind energy harvesting across a wider range of wind speeds in different directions.

CRediT authorship contribution statement

Cuipeng Xia: Writing – review & editing, Writing – original draft, Software, Methodology, Investigation, Formal analysis, Data curation, Conceptualization. **Lihua Tang:** Writing – review & editing, Supervision, Methodology. **Yi Wu:** Writing – review & editing, Methodology. **Guobiao Hu:** Methodology. **Peilun Yin:** Writing – review & editing. **Kean C. Aw:** Writing – review & editing, Supervision. **Daniel J. Inman:** Writing – review & editing.

Declaration of competing interest

The authors declare that they have no known competing financial interests or personal relationships that could have appeared to influence the work reported in this paper.

Acknowledgments

This work was financially supported by a PhD scholarship from the China Scholarship Council (No. 202207000016).

Appendix A

The area and mass per unit length of each beam segment can be expressed as:

$$A_1 = A_\mathrm{p} + A_\mathrm{s1} = 2b_\mathrm{p}d_\mathrm{p} + b_\mathrm{s}d_\mathrm{s}, A_2 = A_3 = A_4 = b_\mathrm{s}d_\mathrm{s} \tag{A.1}$$

$$m_1 = A_\mathrm{p}\rho_\mathrm{p} + A_\mathrm{s1}\rho_\mathrm{s} = 2b_\mathrm{p}d_\mathrm{p}\rho_\mathrm{p} + b_\mathrm{s}d_\mathrm{s}\rho_\mathrm{s}, m_2 = m_3 = m_4 = b_\mathrm{s}d_\mathrm{s}\rho_\mathrm{s} \tag{A.2}$$

For the beam segment covered with piezoelectric transducers, the distance from the neutral axis to the top of the substrate layer of the beam and the distance from the neutral axis to the bottom of piezoelectric transducer of the beam can be expressed as:

$$h_\mathrm{pn} = \frac{2d_\mathrm{p}^2 + 2nd_\mathrm{s}d_\mathrm{p} + nd_\mathrm{s}^2}{2(2d_\mathrm{p} + nd_\mathrm{s})}, h_\mathrm{sn} = \frac{2d_\mathrm{p}^2 + 4d_\mathrm{p}d_\mathrm{s} + nd_\mathrm{s}^2}{4d_\mathrm{p} + 2nd_\mathrm{s}} \tag{A.3}$$

where $n = E_s/E_p$ is the Young's moduli ratio between the substrate layer of the beam and piezoelectric transducer. Note that the geometric parameters used in the main formulation h_a, h_b, and h_c describe the positions from the neutral axis rather than distances. They can be expressed as

$$h_{\mathrm{a}} = -h_{\mathrm{pn}}, h_{\mathrm{b}} = h_{\mathrm{pn}} - d_{\mathrm{p}}, h_{\mathrm{c}} = h_{\mathrm{sn}} \qquad \text{(A.4)}$$

h_a is the position of the bottom of the piezoelectric transducer layer from the neutral axis, h_b is the position of the bottom of the substructure layer from the neutral axis, and h_c is the position of the top of the substructure layer from the neutral axis. The area moment of inertia of the cross-sectional areas of the beam segments can be expressed as:

$$I_{\mathrm{p}} = 2\iint_{A_{\mathrm{p}}} z^2 dA = \frac{2b_{\mathrm{p}}\left(h_{\mathrm{b}}^3 - h_{\mathrm{a}}^3\right)}{3}, I_{\mathrm{s1}} = \iint_{A_{\mathrm{s}}} z^2 dA = \frac{b_{\mathrm{s}}\left(h_{\mathrm{c}}^3 - h_{\mathrm{b}}^3\right)}{3}, I_i = \frac{b_{\mathrm{s}} d_{\mathrm{s}}^3}{12} \quad (i = 2, 3, 4) \qquad \text{(A.5)}$$

The bending stiffness of the beam segments can then be given as:

$$E_1 I_1 = E_{\mathrm{p}} I_{\mathrm{p}} + E_{\mathrm{s}} I_{\mathrm{s1}} = \frac{2E_{\mathrm{p}} b_{\mathrm{p}}\left(h_{\mathrm{b}}^3 - h_{\mathrm{a}}^3\right) + E_{\mathrm{s}} b_{\mathrm{s}}\left(h_{\mathrm{c}}^3 - h_{\mathrm{b}}^3\right)}{3}, E_i I_i = \frac{E_{\mathrm{s}} b_{\mathrm{s}} d_{\mathrm{s}}^3}{12} \quad (i = 2, 3, 4) \qquad \text{(A.6)}$$

Appendix B. 1

Simultaneous equations from boundary conditions in the modal analysis:

$$\phi_{1r}(0) = 0 \qquad \text{1.1)}$$

$$\phi'_{1r}(0) = 0 \qquad \text{1.2)}$$

$$\phi_{1r}(L_1) = \phi_{2r}(0) \qquad \text{1.3)}$$

$$a_{1r}(\sin\beta_{1r}L_1) + b_{1r}(\cos\beta_{1r}L_1) + c_{1r}(\sinh\beta_{1r}L_1) + d_{1r}(\cosh\beta_{1r}L_1) - b_{2r} - d_{2r} = 0 \qquad \text{1.4)}$$

$$\phi'_{1r}(L_1) = \phi'_{2r}(0) \qquad \text{1.5)}$$

$$\beta_{1r}(a_{1r}\cos\beta_{1r}L_1 - b_{1r}\sin\beta_{1r}L_1 + c_{1r}\cosh\beta_{1r}L_1 + d_{1r}\sinh\beta_{1r}L_1) - \beta_{2r}(a_{2r} + c_{2r}) = 0 \qquad \text{1.6)}$$

$$E_1 I_1 \phi''_{1r}(L_1) = E_2 I_2 \phi''_{2r}(0) \qquad \text{1.7)}$$

$$E_1 I_1 \beta_{1r}^2(-a_{1r}\sin\beta_{1r}L_1 - b_{1r}\cos\beta_{1r}L_1 + c_{1r}\sinh\beta_{1r}L_1 + d_{1r}\cosh\beta_{1r}L_1) + b_{2r} - d_{2r} = 0 \qquad \text{1.8)}$$

$$E_1 I_1 \phi'''_{1r}(L_1) = E_2 I_2 \phi'''_{2r}(0) \qquad \text{1.9)}$$

$$E_1 I_1 \beta_{1r}^3(-a_{1r}\cos\beta_{1r}L_1 + b_{1r}\sin\beta_{1r}L_1 + c_{1r}\cosh\beta_{1r}L_1 + d_{1r}\sinh\beta_{1r}L_1) + a_{2r} - c_{2r} = 0 \qquad \text{1.10)}$$

$$\phi_{2r}(L_2) = -\phi_{2r}(0) \cdot \cos\varphi - \psi_{2r}(0) \cdot \sin\varphi \qquad \text{1.11)}$$

$$a_{2r}\sin\beta_{2r}L_2 + b_{2r}\cos\beta_{2r}L_2 + c_{2r}\sinh\beta_{2r}L_2 + d_{2r}\cosh\beta_{2r}L_2 + (b_{3r} + d_{3r})\cos\varphi + h_{3r}\sin\varphi = 0 \qquad \text{1.12)}$$

$$\phi'_{2r}(L_2) = \phi'_{3r}(0) \qquad \text{13)}$$

$$\beta_{2r}(a_{2r}\cos\beta_{2r}L_2 - b_{2r}\sin\beta_{2r}L_2 + c_{2r}\cosh\beta_{2r}L_2 + d_{2r}\sinh\beta_{2r}L_2) - \beta_{3r}(a_{3r} + c_{3r}) = 0 \qquad \text{1.14)}$$

$$E_2 I_2 \phi''_{2r}(L_2) = E_3 I_3 \phi''_{3r}(0) \qquad \text{1.15)}$$

$$E_2 I_2 \beta_{2r}^2(-a_{2r}\sin\beta_{2r}L_2 - b_{2r}\cos\beta_{2r}L_2 + c_{2r}\sinh\beta_{2r}L_2 + d_{2r}\cosh\beta_{2r}L_2) + E_3 I_3 \beta_{3r}^2(b_{3r} - d_{3r}) = 0 \qquad \text{1.16)}$$

$$E_2 I_2 \phi'''_{2r}(L_2) = E_3 A_3 \psi'_{3r}(0) \cdot \sin\varphi - E_3 I_3 \phi'''_{3r}(0) \cdot \cos\varphi \qquad \text{1.17)}$$

$$\begin{aligned} &E_2 I_2 \beta_{2r}^3(-a_{2r}\cos\beta_{2r}L_2 + b_{2r}\sin\beta_{2r}L_2 + c_{2r}\cosh\beta_{2r}L_2 + d_{2r}\sinh\beta_{2r}L_2) \\ &\qquad = g_{3r}\delta_{3r}E_3 A_3 \sin\varphi + (a_{3r} - c_{3r})E_3 I_3 \beta_{3r}^3 \cos\varphi \end{aligned} \qquad \text{1.18)}$$

$$\phi_{3r}(L_3) = -\phi_{4r}(0) \cdot \cos\varphi - \psi_{4r}(0) \cdot \sin\varphi \qquad \text{1.19)}$$

$$a_{3r}\sin\beta_{3r}L_3 + b_{3r}\cos\beta_{3r}L_3 + c_{3r}\sinh\beta_{3r}L_3 + d_{3r}\cosh\beta_{3r}L_3 + (b_{4r} + d_{4r})\cos\varphi + h_{4r}\sin\varphi = 0 \tag*{1.20)}$$

$$\phi'_{3r}(L_3) = \phi'_{4r}(0) \tag*{1.21)}$$

$$\beta_{3r}(a_{3r}\cos\beta_{3r}L_3 - b_{3r}\sin\beta_{3r}L_3 + c_{3r}\cosh\beta_{3r}L_3 + d_{3r}\sinh\beta_{3r}L_3) - \beta_{4r}(a_{4r} + c_{4r}) = 0 \tag*{1.22)}$$

$$E_3I_3\phi''_{3r}(L_3) = E_4I_4\phi''_{4r}(0) \tag*{1.23)}$$

$$E_3I_3\beta_{3r}^2(-a_{3r}\sin\beta_{3r}L_3 - b_{3r}\cos\beta_{3r}L_3 + c_{3r}\sinh\beta_{3r}L_3 + d_{3r}\cosh\beta_{3r}L_3) + (b_{4r} - d_{4r})E_4I_4\beta_{4r}^2 = 0 \tag*{1.24)}$$

$$E_3I_3\phi'''_{3r}(L_3) = E_4A_4\psi'_{4r}(0)\cdot\sin\varphi - E_4I_4\phi'''_{4r}(0)\cdot\cos\varphi \tag*{1.25)}$$

$$\begin{aligned}&E_3I_3\beta_{3r}^3(-a_{3r}\cos\beta_{3r}L_3 + b_{3r}\sin\beta_{3r}L_3 + c_{3r}\cosh\beta_{3r}L_3 + d_{3r}\sinh\beta_{3r}L_3)\\&\qquad = g_{4r}\delta_{4r}E_4A_4\sin\varphi + (a_{4r} - c_{4r})E_4I_4\beta_{4r}^3\cos\varphi\end{aligned} \tag*{1.26)}$$

$$E_4I_4\phi''_{4r}(L_4) = J_t\omega_r^2\phi'_{4r}(L_4) \tag*{1.27)}$$

$$\begin{aligned}&(-a_{4r}\sin\beta_{4r}L_4 - b_{4r}\cos\beta_{4r}L_4 + c_{4r}\sinh\beta_{4r}L_4 + d_{4r}\cosh\beta_{4r}L_4)\\&= J_t\frac{\beta_{4r}^3}{m_4}(a_{4r}\cos\beta_{4r}L_4 - b_{4r}\sin\beta_{4r}L_4 + c_{4r}\cosh\beta_{4r}L_4 + d_{4r}\sinh\beta_{4r}L_4)\end{aligned} \tag*{1.28)}$$

$$E_4I_4\phi'''_{4r}(L_4) = -M_t\omega_r^2\phi_{4r}(L_4) \tag*{1.29)}$$

$$\begin{aligned}&(-a_{4r}\cos\beta_{4r}L_4 + b_{4r}\sin\beta_{4r}L_4 + c_{4r}\cosh\beta_{4r}L_4 + d_{4r}\sinh\beta_{4r}L_4)\\&= -\frac{\beta_{4r}M_t}{m_4}(a_{4r}\sin\beta_{4r}L_4 + b_{4r}\cos\beta_{4r}L_4 + c_{4r}\sinh\beta_{4r}L_4 + d_{4r}\cosh\beta_{4r}L_4)\end{aligned} \tag*{1.30)}$$

$$\psi_{1r}(0) = 0 \tag*{1.31)}$$

$$\psi_{1r}(L_1) = \psi_{2r}(0) \tag*{1.32)}$$

$$g_{1r}\sin\delta_{1r}L_1 + h_{1r}\cos\delta_{1r}L_1 - h_{2r} = 0 \tag*{1.33)}$$

$$E_1A_1\psi'_{1r}(L_1) = E_2A_2\psi'_{2r}(0) \tag*{1.34)}$$

$$E_1\delta_{1r}A_1(g_{1r}\cos\delta_{1r}L_1 - h_{1r}\sin\delta_{1r}L_1) - g_{2r}E_2\delta_{2r}A_2 = 0 \tag*{1.35)}$$

$$\psi_{2r}(L_2) = -\psi_{3r}(0)\cdot\cos\varphi + \phi_{3r}(0)\cdot\sin\varphi \tag*{1.36)}$$

$$g_{2r}\sin\delta_{2r}L_2 + h_{2r}\cos\delta_{2r}L_2 + h_{3r}\cos\varphi - (b_{3r} + d_{3r})\sin\varphi = 0 \tag*{1.37)}$$

$$E_2A_2\psi'_{2r}(L_2) = -E_3I_3\phi'''_{3r}(0)\cdot\sin\varphi - E_3A_3\psi'_{3r}(0)\cdot\cos\varphi \tag*{1.38)}$$

$$E_2A_2\delta_{2r}(g_{2r}\cos\delta_{2r}L_2 - h_{2r}\sin\delta_{2r}L_2) - (a_{3r} - c_{3r})E_3I_3\beta_{3r}^3\sin\varphi + g_{3r}E_3A_3\delta_{3r}\cos\varphi = 0 \tag*{1.39)}$$

$$\psi_{3r}(L_3) = -\psi_{4r}(0)\cdot\cos\varphi + \phi_{4r}(0)\cdot\sin\varphi \tag*{1.40)}$$

$$g_{3r}\sin\delta_{3r}L_3 + h_{3r}\cos\delta_{3r}L_3 + h_{4r}\cos\varphi - (b_{4r} + d_{4r})\sin\varphi = 0 \tag*{1.41)}$$

$$E_3A_3\psi'_{3r}(L_3) = -E_4I_4\phi'''_{4r}(0)\cdot\sin\varphi - E_4A_4\psi'_{4r}(0)\cdot\cos\varphi \tag*{1.42)}$$

$$E_3A_3\delta_{3r}\left(g_{3r}\cos\delta_{3r}L_3 - h_{3r}\sin\delta_{3r}L_3\right) - E_4I_4\beta_{4r}^3(a_{4r} - c_{4r})\sin\varphi + g_{4r}E_4A_4\delta_{4r}\cos\varphi = 0 \tag*{1.43)}$$

$$E_4A_4\psi'_{4r}(L_4) = -\omega_r^2M_t\psi_{4r}(L_4) \tag*{1.44)}$$

$$E_4A_4\delta_{4r}\left(g_{4r}\cos\delta_{4r}L_4 - h_{4r}\sin\delta_{4r}L_4\right) = -\frac{\delta_{4r}^2E_4A_4}{m_4}M_t\left(g_{4r}\sin\delta_{4r}L_4 + h_{4r}\cos\delta_{4r}L_4\right) \tag*{1.45)}$$

Appendix B. 2

The matrix of $\mathbf{H}(\omega)$

$$\begin{gathered} h_{12} = h_{14} = h_{21} = h_{23} = h_{56} = h_{65} = h_{9\_10} = h_{10\_9} = h_{13\_14} = h_{14\_13} = h_{17\_18} = h_{20\_10} \\ = h_{20\_12} = h_{21\_9} = h_{22\_14} = h_{22\_16} = h_{23\_13} = 1 \end{gathered} \qquad 2.1)$$

$$\begin{gathered} h_{36} = h_{38} = h_{21} = h_{45} = h_{47} = h_{58} = h_{67} = h_{7\_10} = h_{7\_12} = h_{89} = h_{8\_11} = h_{9\_12} = h_{10\_11} \\ = h_{11\_14} = h_{11\_16} = h_{12\_13} = h_{12\_15} = h_{13\_16} = h_{14\_15} = h_{18\_20} = h_{21\_11} = h_{23\_15} = -1 \end{gathered} \qquad 2.2)$$

$$h_{31} = \sin\beta_{1r}L_1, h_{32} = \cos\beta_{1r}L_1, h_{33} = \sinh\beta_{1r}L_1, h_{34} = \cosh\beta_{1r}L_1 \qquad 2.3)$$

$$h_{41} = R_1\cos\beta_{1r}L_1, h_{42} = -R_1\sin\beta_{1r}L_1, h_{43} = R_1\cosh\beta_{1r}L_1, h_{44} = R_1\sinh\beta_{1r}L_1 \qquad 2.4)$$

$$h_{51} = -R_2\sin\beta_{1r}L_1, h_{52} = -R_2\cos\beta_{1r}L_1, h_{53} = R_2\sinh\beta_{1r}L_1, h_{54} = R_2\cosh\beta_{1r}L_1 \qquad 2.5)$$

$$h_{61} = -R_3\cos\beta_{1r}L_1, h_{62} = R_3\sin\beta_{1r}L_1, h_{63} = R_3\cosh\beta_{1r}L_1, h_{64} = R_3\sinh\beta_{1r}L_1 \qquad 2.6)$$

$$h_{75} = \frac{\sin\beta_{2r}L_2}{-\cos\varphi}, h_{76} = \frac{\cos\beta_{2r}L_2}{-\cos\varphi}, h_{77} = \frac{\sinh\beta_{2r}L_2}{-\cos\varphi}, h_{78} = \frac{\cosh\beta_{2r}L_2}{-\cos\varphi}, h_{7\_22} = -\tan\varphi \qquad 2.7)$$

$$h_{85} = R_4\cos\beta_{2r}L_2, h_{86} = -R_4\sin\beta_{2r}L_2, h_{87} = R_4\cosh\beta_{2r}L_2, h_{88} = R_4\sinh\beta_{2r}L_2 \qquad 2.8)$$

$$h_{95} = -R_5\sin\beta_{2r}L_2, h_{96} = -R_5\cos\beta_{2r}L_2, h_{97} = R_5\sinh\beta_{2r}L_2, h_{98} = R_5\cosh\beta_{2r}L_2 \qquad 2.9)$$

$$\begin{gathered} h_{10\_5} = \frac{R_6\cos\beta_{2r}L_2}{\cos\varphi}, h_{10\_6} = \frac{R_6\sin\beta_{2r}L_2}{-\cos\varphi}, h_{10\_7} = \frac{R_6\cosh\beta_{2r}L_2}{-\cos\varphi}, h_{10\_8} = \frac{R_6\sinh\beta_{2r}L_2}{-\cos\varphi} \\ h_{10\_21} = \frac{A_3\delta_{3r}}{I_3\beta_{3r}^3}\cdot\tan\varphi \end{gathered} \qquad 2.10)$$

$$h_{11\_9} = \frac{\sin\beta_{3r}L_3}{-\cos\varphi}, h_{11\_10} = \frac{\cos\beta_{3r}L_3}{-\cos\varphi}, h_{11\_11} = \frac{\sinh\beta_{3r}L_3}{-\cos\varphi}, h_{11\_12} = \frac{\cosh\beta_{3r}L_3}{-\cos\varphi}, h_{11\_24} = -\tan\varphi \qquad 2.11)$$

$$h_{12\_9} = R_7\cos\beta_{3r}L_3, h_{12\_10} = -R_7\sin\beta_{3r}L_3, h_{12\_11} = R_7\cosh\beta_{3r}L_3, h_{12\_12} = R_7\sinh\beta_{3r}L_3 \qquad 2.12)$$

$$h_{13\_9} = -R_8\sin\beta_{3r}L_3, h_{13\_10} = -R_8\cos\beta_{3r}L_3, h_{13\_11} = R_8\sinh\beta_{3r}L_3, h_{13\_12} = R_8\cosh\beta_{3r}L_3 \qquad 2.13)$$

$$\begin{gathered} h_{14\_9} = \frac{R_9\cos\beta_{3r}L_3}{\cos\varphi}, h_{14\_10} = \frac{R_9\sin\beta_{3r}L_3}{-\cos\varphi}, h_{14\_11} = \frac{R_9\cosh\beta_{3r}L_3}{-\cos\varphi}, h_{14\_12} = \frac{R_9\sinh\beta_{3r}L_3}{-\cos\varphi}, \\ h_{14\_23} = \frac{A_4\delta_{4r}\tan\varphi}{I_4\beta_{4r}^3} \end{gathered} \qquad 2.14)$$

$$\begin{gathered} h_{15\_13} = -\sin\beta_{4r}L_4 - J_t\frac{\beta_{4r}^3}{m_4}\cos\beta_{4r}L_4, h_{15\_14} = -\cos\beta_{4r}L_4 + J_t\frac{\beta_{4r}^3}{m_4}\sin\beta_4L_4, \\ h_{15\_15} = \sinh\beta_{4r}L_4 - J_t\frac{\beta_{4r}^3}{m_4}\cosh\beta_{4r}L_4, h_{15\_16} = \cosh\beta_{4r}L_4 - J_t\frac{\beta_{4r}^3}{m_4}\sinh\beta_{4r}L_4 \end{gathered} \qquad 2.15)$$

$$\begin{gathered} h_{16\_13} = -\cos\beta_{4r}L_4 + \frac{\beta_{4r}M_t}{m_4}\sin\beta_{4r}L_4, h_{16\_14} = \sin\beta_{4r}L_4 + \frac{\beta_{4r}M_t}{m_4}\cos\beta_{4r}L_4, \\ h_{16\_15} = \cosh\beta_{4r}L_4 + \frac{\beta_{4r}M_t}{m_4}\sinh\beta_{4r}L_4, h_{16\_16} = \sinh\beta_{4r}L_4 + \frac{\beta_{4r}M_t}{m_4}\cosh\beta_{4r}L_4 \end{gathered} \qquad 2.16)$$

$$h_{18\_17} = \sin\delta_{1r}L_1, h_{18\_18} = \cos\delta_{1r}L_1 \qquad 2.17)$$

$$h_{19\_17} = E_1A_1\delta_{1r}\cos\delta_{1r}L_1, h_{19\_18} = -E_1A_1\delta_{1r}\sin\delta_{1r}L_1, h_{19\_19} = -E_2A_2\delta_{2r} \qquad 2.18)$$

$$h_{20\_19} = -\frac{\sin\delta_{2r}L_2}{\sin\varphi}, h_{20\_20} = -\frac{\cos\delta_{2r}L_2}{\sin\varphi}, h_{20\_22} = -\cot\varphi \qquad 2.19)$$

$$h_{21\_19} = -\frac{E_2A_2\delta_{2r}}{E_3I_3\beta_{3r}^3}\cdot\frac{\cos\delta_{2r}L_2}{\sin\varphi}, h_{21\_20} = \frac{E_2A_2\delta_{2r}}{E_3I_3\beta_{3r}^3}\cdot\frac{\sin\delta_{2r}L_2}{\sin\varphi}, h_{21\_21} = -\frac{A_3\delta_{3r}}{I_3\beta_{3r}^3}\cdot\cot\varphi \qquad 2.20)$$

$$h_{22\_21} = -\frac{\sin\delta_{3r}L_3}{\sin\varphi}, h_{22\_22} = -\frac{\cos\delta_{3r}L_3}{\sin\varphi}, h_{22\_24} = -\cot\varphi \tag*{2.21)}$$

$$h_{23\_21} = -\frac{E_3A_3\delta_{3r}}{E_4I_4\beta_{4r}^3}\cdot\frac{\cos\delta_{3r}L_3}{\sin\varphi}, h_{23\_22} = \frac{E_3A_3\delta_{3r}}{E_4I_4\beta_{4r}^3}\cdot\frac{\sin\delta_{3r}L_3}{\sin\varphi}, h_{23\_23} = \frac{A_4\delta_{4r}}{I_4\beta_{4r}^3}\cdot\cot\varphi \tag*{2.22)}$$

$$h_{24\_23} = \cos\delta_{4r}L_4 + \frac{\delta_{4r}M_t}{m_4}\sin\delta_{4r}L_4, h_{24\_24} = -\sin\delta_{4r}L_4 + \frac{\delta_{4r}M_t}{m_4}\cos\delta_{4r}L_4 \tag*{2.23)}$$

$$\begin{aligned}
R_1 &= \frac{\beta_{1r}}{\beta_{2r}} = \sqrt[4]{\frac{E_2I_2m_1}{E_1I_1m_2}}, R_2 = \frac{\beta_{1r}^2E_1I_1}{\beta_{2r}^2E_2I_2} = \sqrt{\frac{E_1I_1m_1}{E_2I_2m_2}}, R_3 = \frac{\beta_{1r}^3E_1I_1}{\beta_{2r}^3E_2I_2} = \frac{(E_1I_1)^{1/4}m_1^{3/4}}{(E_2I_2)^{1/4}m_2^{3/4}},\\
R_4 &= \frac{\beta_{2r}}{\beta_{3r}} = \sqrt[4]{\frac{E_3I_3m_2}{E_2I_2m_3}}, R_5 = \frac{\beta_{2r}^2E_2I_2}{\beta_{3r}^2E_3I_3} = \sqrt{\frac{E_2I_2m_2}{E_3I_3m_3}}, R_6 = \frac{\beta_{2r}^3E_2I_2}{\beta_{3r}^3E_3I_3} = \frac{(E_2I_2)^{1/4}m_2^{3/4}}{(E_3I_3)^{1/4}m_3^{3/4}},\\
R_7 &= \frac{\beta_{3r}}{\beta_{4r}} = \sqrt[4]{\frac{E_4I_4m_3}{E_3I_3m_4}}, R_8 = \frac{\beta_{3r}^2E_3I_3}{\beta_{4r}^2E_4I_4} = \sqrt{\frac{E_3I_3m_3}{E_4I_4m_4}}, R_9 = \frac{\beta_{3r}^3E_3I_3}{\beta_{4r}^3E_4I_4} = \frac{(E_3I_3)^{1/4}m_3^{3/4}}{(E_4I_4)^{1/4}m_4^{3/4}}
\end{aligned} \tag*{2.24)}$$

$$\delta_{1r} = \beta_{1r}^2\sqrt{\frac{I_1}{A_1}}, \delta_{2r} = \beta_{2r}^2\sqrt{\frac{I_2}{A_2}}, \delta_{3r} = \beta_{3r}^2\sqrt{\frac{I_3}{A_3}}, \delta_{4r} = \beta_{4r}^2\sqrt{\frac{I_4}{A_4}} \tag*{2.25)}$$

Appendix C

Parameters in aero-electro-mechanical governing equations:

$$\left\{\begin{array}{l}
\widetilde{\lambda}_1 = \widetilde{\chi}_1^b - \widetilde{\chi}_1^a\\
\widetilde{\lambda}_2 = \widetilde{\chi}_2^b - \widetilde{\chi}_2^a
\end{array}\right. \tag{C1}$$

$$\left\{\begin{array}{c}
\widetilde{M}_1 = \sum_{i=1}^4 m_{11}^{aai} - 2\sum_{i=1}^4 m_{11}^{abi} + \sum_{i=1}^4 m_{11}^{bbi}\\
\widetilde{K}_1 = \sum_{i=1}^4 k_{11}^{aai} - 2\sum_{i=1}^4 k_{11}^{abi} + \sum_{i=1}^4 k_{11}^{bbi}\\
\widetilde{C}_1 = \widehat{a}_0\widetilde{M}_1 + \widehat{a}_1\widetilde{K}_1
\end{array}\right.
\left\{\begin{array}{c}
\widetilde{M}_2 = \sum_{i=1}^4 m_{22}^{aai} - 2\sum_{i=1}^4 m_{22}^{abi} + \sum_{i=1}^4 m_{22}^{bbi}\\
\widetilde{K}_2 = \sum_{i=1}^4 k_{22}^{aai} - 2\sum_{i=1}^4 k_{22}^{abi} + \sum_{i=1}^4 k_{22}^{bbi}\\
\widetilde{C}_2 = \widehat{a}_0\widetilde{M}_2 + \widehat{a}_1\widetilde{K}_2
\end{array}\right. \tag{C2}$$

$$\left\{\begin{array}{c}\widehat{a}_0\\ \widehat{a}_1\end{array}\right\} = \frac{2\omega_1\omega_2}{\omega_2^2-\omega_1^2}\begin{bmatrix}\omega_2 & -\omega_1\\ -\dfrac{1}{\omega_2} & \dfrac{1}{\omega_1}\end{bmatrix}\left\{\begin{array}{c}\xi_1\\ \xi_2\end{array}\right\} \tag{C3}$$

where the $\widehat{a}_0$ and $\widehat{a}_1$ are the mass-proportional and stiffness proportional damping coefficients, respectively. These coefficients have been conventionally evaluated from two damping ratios (ξ_1 and ξ_2) and natural frequencies (ω_1 and ω_2) corresponding to first and second order bending modes of vibration, respectively.

$$\widetilde{F}_1 = (\phi_{41}(L_4)\cos\theta + \psi_{41}(L_4)\sin\theta)\frac{1}{2}\rho hlU^2\sum_{i=1,3,5}C_i\left(\frac{\dot{q}_1(t)(\phi_{41}(L_4)\cos\theta + \psi_{41}(L_4)\sin\theta)}{U} + q_1(t)\phi_{41}'(L_4)\right)^i \tag{C4}$$

$$\widetilde{F}_2 = (\phi_{42}(L_4)\cos\theta + \psi_{42}(L_4)\sin\theta)\frac{1}{2}\rho hlU^2\sum_{i=1,3,5}C_i\left(\frac{\dot{q}_2(t)(\phi_{42}(L_4)\cos\theta + \psi_{42}(L_4)\sin\theta)}{U} + q_2(t)\phi_{42}'(L_4)\right)^i \tag{C5}$$

Data availability

Data will be made available on request.

References

[1] Y. Hu, B. Yang, X. Chen, X. Wang, J. Liu, Modeling and experimental study of a piezoelectric energy harvester from vortex shedding-induced vibration, Energ. Conver. Manage. 162 (2018) 145–158.
[2] M.A.A. Abdelkareem, X. Jing, A.B.M. Eldaly, Y. Choy, 3-DOF X-structured piezoelectric harvesters for multidirectional low-frequency vibration energy harvesting, Mech. Syst. Sig. Process. 200 (2023).
[3] K. Chen, Q. Gao, S. Fang, D. Zou, Z. Yang, W.-H. Liao, An auxetic nonlinear piezoelectric energy harvester for enhancing efficiency and bandwidth, Appl. Energy 298 (2021).
[4] Z. Xie, W. Zhu, An investigation on the lubrication characteristics of floating ring bearing with consideration of multi-coupling factors, Mech. Syst. Sig. Process. 162 (2022).
[5] B. Vysotskyi, J.-F. Ambia Campos, E. Lefeuvre, A. Brenes, Dynamic analysis of a novel two-sided nonlinear MEMS electrostatic energy harvester, Mech. Syst. Sig. Process. 206 (2024).
[6] M. Toghyani, A. Saadat, From challenge to opportunity: Enhancing oil refinery plants with sustainable hybrid renewable energy integration, Energ. Conver. Manage. 305 (2024).
[7] K. Kecik, Assessment of energy harvesting and vibration mitigation of a pendulum dynamic absorber, Mech. Syst. Sig. Process. 106 (2018) 198–209.
[8] M.A.A. Abdelkareem, L. Xu, M.K.A. Ali, A. Elagouz, J. Mi, S. Guo, Y. Liu, L. Zuo, Vibration energy harvesting in automotive suspension system: A detailed review, Appl. Energy 229 (2018) 672–699.
[9] L. He, H. Kurita, F. Narita, Multimode auxetic piezoelectric energy harvester for low-frequency vibration, Smart Mater. Struct. 33 (2024).
[10] T. Wang, H. Wang, D. Yang, B. Tan, S. Deng, G. Lu, Early bolt looseness monitoring using the leading waves energy in piezoelectric active sensing, Smart Mater. Struct. 33 (2024).
[11] Z. Abdin, W. Mérida, Hybrid energy systems for off-grid power supply and hydrogen production based on renewable energy: A techno-economic analysis, Energ. Conver. Manage. 196 (2019) 1068–1079.
[12] B. Su, Y. Wang, J. Li, T. Guo, G. Cheng, W. Sun, A novel elastic strip suspension-based bi-directional electromagnetic wind energy harvester designed specifically for wind energy factories, Mech. Syst. Sig. Process. 208 (2024).
[13] A. Kasaeian, P. Rahdan, M.A.V. Rad, W.-M. Yan, Optimal design and technical analysis of a grid-connected hybrid photovoltaic/diesel/biogas under different economic conditions: A case study, Energ. Conver. Manage. 198 (2019).
[14] G. Sebald, D. Guyomar, A. Agbossou, On thermoelectric and pyroelectric energy harvesting, Smart Mater. Struct. 18 (2009).
[15] P. Yin, H. Han, L. Tang, X. Tan, M. Guo, C. Xia, K.C. Aw, Kresling origami-inspired electromagnetic energy harvester with reversible nonlinearity, Smart Mater. Struct. 33 (2024).
[16] Y. Han, C. Wang, L. Sun, H. Wang, B. Yang, L. He, Research on a rotary piezoelectric energy harvester based on movable magnets, Smart Mater. Struct. 33 (2024).
[17] Y. Xu, T. Xian, C. Chen, G. Wang, M. Wang, W. Shi, Mathematical modeling and parameter optimization of a stacked piezoelectric energy harvester based on water pressure pulsation, Energy 292 (2024).
[18] H.-H. Chen, S.-K. You, W.-J. Su, The design, fabrication and analysis of a cantilever-based tensile-mode nonlinear piezoelectric energy harvester, Mech. Syst. Sig. Process. 212 (2024).
[19] P. Yin, L. Tang, Z. Li, H. Guo, K.C. Aw, Circuit representation, experiment and analysis of parallel-cell triboelectric nanogenerator, Energ. Conver. Manage. 278 (2023).
[20] Z. Li, W.C. Gan, L. Tang, K.C. Aw, Fundamental Understanding of Multicellular Triboelectric Nanogenerator with Different Electrical Configurations, Micromachines (basel) 14 (2023).
[21] P. Yin, K.C. Aw, X. Jiang, C. Xin, H. Guo, L. Tang, Y. Peng, Z. Li, Fish gills inspired parallel-cell triboelectric nanogenerator, Nano Energy 95 (2022).
[22] X. Li, D. Upadrashta, K. Yu, Y. Yang, Analytical modeling and validation of multi-mode piezoelectric energy harvester, Mech. Syst. Sig. Process. 124 (2019) 613–631.
[23] S. Dhote, Z. Yang, J. Zu, Modeling and experimental parametric study of a tri-leg compliant orthoplanar spring based multi-mode piezoelectric energy harvester, Mech. Syst. Sig. Process. 98 (2018) 268–280.
[24] X. Nie, T. Tan, Z. Yan, Z. Yan, M.R. Hajj, Broadband and high-efficient L-shaped piezoelectric energy harvester based on internal resonance, Int. J. Mech. Sci. 159 (2019) 287–305.
[25] H. Li, D. Liu, J. Wang, X. Shang, M.R. Hajj, Broadband bimorph piezoelectric energy harvesting by exploiting bending-torsion of L-shaped structure, Energ. Conver. Manage. 206 (2020).
[26] J.W. Xu, Y.B. Liu, W.W. Shao, Z. Feng, Optimization of a right-angle piezoelectric cantilever using auxiliary beams with different stiffness levels for vibration energy harvesting, Smart Mater. Struct. 21 (2012).
[27] X. Nie, T. Tan, Z. Yan, Z. Yan, W. Zhang, Ultra-wideband piezoelectric energy harvester based on Stockbridge damper and its application in smart grid, Appl. Energy 267 (2020).
[28] J.W. Xu, W.W. Shao, F.R. Kong, Z.H. Feng, Right-angle piezoelectric cantilever with improved energy harvesting efficiency, Appl. Phys. Lett. 96 (2010).
[29] V.J. Caetano, M.A. Savi, Star-shaped piezoelectric mechanical energy harvesters for multidirectional sources, Int. J. Mech. Sci. 215 (2022).
[30] X. Zhang, J. Hu, Q. Yang, H. Yang, H. Yang, Q. Li, X. Li, C. Hu, Y. Xi, Z.L. Wang, Harvesting Multidirectional Breeze Energy and Self-Powered Intelligent Fire Detection Systems Based on Triboelectric Nanogenerator and Fluid-Dynamic Modeling, Adv. Funct. Mater. 31 (2021).
[31] S. Zhou, J.D. Hobeck, J. Cao, D.J. Inman, Analytical and experimental investigation of flexible longitudinal zigzag structures for enhanced multi-directional energy harvesting, Smart Mater. Struct. 26 (2017).
[32] W.-J. Su, J. Zu, An innovative tri-directional broadband piezoelectric energy harvester, Appl. Phys. Lett. 103 (2013).
[33] B. Bao, S. Zhou, Q. Wang, Interplay between internal resonance and nonlinear magnetic interaction for multi-directional energy harvesting, Energ. Conver. Manage. 244 (2021).
[34] Y. Wu, J. Qiu, S. Zhou, H. Ji, Y. Chen, S. Li, A piezoelectric spring pendulum oscillator used for multi-directional and ultra-low frequency vibration energy harvesting, Appl. Energy 231 (2018) 600–614.
[35] J. Xing, X. Ji, J. Wu, I. Howard, A body hair-inspired multi-directional piezoelectric energy harvester with spatial internal resonance effect, J. Sound Vib. 589 (2024).
[36] Y. Zhang, G. Zhang, W. Wang, A piezoelectric cantilever-beam-spring-pendulum oscillator for multi-directional vibration energy harvesting, Commun. Nonlinear Sci. Numer. Simul. 138 (2024).
[37] J. Kan, S. Wu, Y. Lin, Z. Kuang, W. Wu, Z. Cao, Z. Zhang, A low-frequency multidirectional piezoelectric vibration energy harvester using a universal joint structure, J. Intell. Mater. Syst. Struct. 35 (2024) 1335–1346.
[38] K. Lu, R. Hu, X. Wang, Z. Deng, Multi-directional and ultra-low frequency energy harvester utilizing tunable buckled piezoelectric film, Mech. Syst. Sig. Process. 210 (2024).
[39] K. Chen, F. Gao, Z. Liu, W.-H. Liao, A nonlinear M-shaped tri-directional piezoelectric energy harvester, Smart Mater. Struct. 30 (2021).
[40] Z. Wu, Q. Xu, Design and testing of a novel bidirectional energy harvester with single piezoelectric stack, Mech. Syst. Sig. Process. 122 (2019) 139–151.
[41] T. Tan, Z. Wang, L. Zhang, W.-H. Liao, Z. Yan, Piezoelectric autoparametric vibration energy harvesting with chaos control feature, Mech. Syst. Sig. Process. 161 (2021).
[42] X. Zeng, N. Wu, J. Fu, Y. He, X. Dai, Design, modeling and experiments of bistable wave energy harvester with directional self-adaptive characteristics, Energy 311 (2024).
[43] S. Chen, L. Zhao, A quasi-zero stiffness two degree-of-freedom nonlinear galloping oscillator for ultra-low wind speed aeroelastic energy harvesting, Appl. Energy 331 (2023).

[44] G. Hu, K.T. Tse, M. Wei, R. Naseer, A. Abdelkefi, K.C.S. Kwok, Experimental investigation on the efficiency of circular cylinder-based wind energy harvester with different rod-shaped attachments, Appl. Energy 226 (2018) 682–689.

[45] F.-R. Liu, W.-M. Zhang, Z.-K. Peng, G. Meng, Fork-shaped bluff body for enhancing the performance of galloping-based wind energy harvester, Energy 183 (2019) 92–105.

[46] F.-R. Liu, W.-M. Zhang, L.-C. Zhao, H.-X. Zou, T. Tan, Z.-K. Peng, G. Meng, Performance enhancement of wind energy harvester utilizing wake flow induced by double upstream flat-plates, Appl. Energy 257 (2020).

[47] C. Zhang, G. Hu, D. Yurchenko, P. Lin, S. Gu, D. Song, H. Peng, J. Wang, Machine learning based prediction of piezoelectric energy harvesting from wake galloping, Mech. Syst. Sig. Process. 160 (2021).

[48] X. Fan, K. Guo, Y. Wang, Toward a high performance and strong resilience wind energy harvester assembly utilizing flow-induced vibration: Role of hysteresis, Energy 251 (2022).

[49] J. Wang, C. Zhang, D. Yurchenko, A. Abdelkefi, M. Zhang, H. Liu, Usefulness of inclined circular cylinders for designing ultra-wide bandwidth piezoelectric energy harvesters: Experiments and computational investigations, Energy 239 (2022).

[50] C. Xia, L. Tang, P. Yin, K.C. Aw, Multi-directional and multi-modal vortex-induced vibrations for wind energy harvesting, Appl. Phys. Lett. 125 (2024).

[51] J. Kan, J. Wang, F. Meng, C. He, S. Li, S. Wang, Z. Zhang, A downwind-vibrating piezoelectric energy harvester under the disturbance of a downstream baffle, Energy 262 (2023).

[52] X. Fan, Y. Wang, W. Tan, Aerodynamic wake oscillator for modeling flow-induced vibration of tandem cylinders with short spans, Int. J. Mech. Sci. 204 (2021).

[53] H. Tian, X. Shan, H. Cao, T. Xie, Enhanced performance of airfoil-based piezoaeroelastic energy harvester: numerical simulation and experimental verification, Mech. Syst. Sig. Process. 162 (2022).

[54] L. Zhao, Y. Yang, Enhanced aeroelastic energy harvesting with a beam stiffener, Smart Mater. Struct. 24 (2015).

[55] X. Huang, T. Zhong, Hydrokinetic energy harvesting from flow-induced vibration of a hollow cylinder attached with a bi-stable energy harvester, Energ. Conver. Manage. 278 (2023).

[56] J. Wang, G. Hu, Z. Su, G. Li, W. Zhao, L. Tang, L. Zhao, A cross-coupled dual-beam for multi-directional energy harvesting from vortex induced vibrations, Smart Mater. Struct. 28 (2019).

[57] W.-J. Su, W.-Y. Lin, Design and analysis of a vortex-induced bi-directional piezoelectric energy harvester, Int. J. Mech. Sci. 173 (2020).

[58] S. Li, X. He, J. Li, Z. Feng, X. Yang, J. Li, An in-plane omnidirectional piezoelectric wind energy harvester based on vortex-induced vibration, Appl. Phys. Lett. 120 (2022).

[59] Y. Gong, X. Shan, X. Luo, J. Pan, T. Xie, Z. Yang, Direction-adaptive energy harvesting with a guide wing under flow-induced oscillations, Energy 187 (2019).

[60] L. Zhang, Y. He, B. Meng, H. Dai, A. Abdelkefi, L. Wang, Omnidirectional wind piezoelectric energy harvesting, J. Phys. D Appl. Phys. 56 (2023).

[61] X.K. Meng, Z. Lu, H.L. Dai, A. Abdelkefi, Comparative experimental investigation and effectiveness of sphere- and cylinder-based piezoelectric energy harvesters, Smart Mater. Struct. 30 (2021).

[62] H. Kim, J. Lee, J. Seok, Novel piezoelectric wind energy harvester based on coupled galloping phenomena with characterization and quantification of its dynamic behavior, Energ. Conver. Manage. 266 (2022).

[63] J. Xing, M. Rezaei, H. Dai, W.-H. Liao, Investigating the effect of surface protrusions on galloping energy harvesting, Appl. Phys. Lett. 122 (2023).

[64] J. Wang, S. Zhou, Z. Zhang, D. Yurchenko, High-performance piezoelectric wind energy harvester with Y-shaped attachments, Energ. Conver. Manage. 181 (2019) 645–652.

[65] J. Wang, L. Tang, L. Zhao, Z. Zhang, Efficiency investigation on energy harvesting from airflows in HVAC system based on galloping of isosceles triangle sectioned bluff bodies, Energy 172 (2019) 1066–1078.

[66] F. Cui, P. Liu, H. Wang, Z. Li, J. Xiang, J. Xu, H. Ren, A simultaneous measurement method for multi-directional galloping of iced bundled conductors and its application in spatial galloping behavior, Meas. Sci. Technol. 35 (2024).

[67] C. Lu, G. Wu, C. Xu, X. Jiang, F. Tian, J. Liu, T. Wang, X. Wang, G. Fu, Multidirectional galloping-based wind energy harvester based on a cylindrical cantilever beam and multi-tooth blunt body, Phys. Scr. 98 (2023).

[68] W. Sun, J. Li, Z. Wang, Y. Zhong, Z. Zhang, G. Cheng, A wind-direction adaptive piezoelectric energy harvester employing small wing passive control configuration, Appl. Phys. Lett. 124 (2024).

[69] Y.Y. Lim, R.V. Padilla, A. Unger, R. Barraza, A.M. Thabet, I. Izadgoshasb, A self-tunable wind energy harvester utilising a piezoelectric cantilever beam with bluff body under transverse galloping for field deployment, Energ. Conver. Manage. 245 (2021).

[70] C. Xia, J. Yang, L. Tang, P. Yin, Z. Li, B. Wang, K.C. Aw, A multi-directional and multi-modal galloping piezoelectric energy harvester with tri-section beam, Smart Mater. Struct. 33 (2024).

[71] J. Wei, D. Cao, L. Liu, W. Huang, Global mode method for dynamic modeling of a flexible-link flexible-joint manipulator with tip mass, App. Math. Model. 48 (2017) 787–805.

[72] B. Fang, Y. Wang, B. Zhu, Y. Wu, Y. Tian, Y. Li, D. Cao, 3D-spatial vibration global modes of a flexible arm-supported ring antenna and its dynamic analysis, App. Math. Model. 123 (2023) 590–626.

[73] Y. Wu, D. Cao, M. Liu, Y. Li, Z. Chen, Natural characteristic and vibration analysis of nonlinear articulated multi-beam ring structure for modeling ring truss antenna under base excitation, App. Math. Model. 108 (2022) 787–806.

[74] J.P. Ray, W. Clough, Dynamics of Structures, McGraw-Hill (1993).

[75] J.P.D. Hartog, Transmission Line Vibration Due to Sleet, Trans. Am. Inst. Electr. Eng. 51 (1932) 1074–1076.

[76] Michael P. Paidoussis, Stuart J. Price, E.d. Langre, Fluid-Structure Interactions: Cross-Flow-Induced Instabilities, Cambridge University Press, 2010.

[77] L. Tang, L. Zhao, Y. Yang, E. Lefeuvre, Equivalent Circuit Representation and Analysis of Galloping-Based Wind Energy Harvesting, IEEE/ASME Trans. Mechatron. 20 (2015) 834–844.